

# Geochemistry of the Volcan de l'Androy Basalt–Rhyolite Complex, Madagascar Cretaceous Igneous Province

J. J. MAHONEY<sup>1\*</sup>, A. D. SAUNDERS<sup>2</sup>, M. STOREY<sup>3</sup> AND A. RANDRIAMANANTENASOA<sup>4</sup>

<sup>1</sup>SCHOOL OF OCEAN AND EARTH SCIENCE AND TECHNOLOGY, UNIVERSITY OF HAWAII, HONOLULU, HI 96822, USA

<sup>2</sup>GEOLOGY DEPARTMENT, UNIVERSITY OF LEICESTER, LEICESTER LE1 7RH, UK

<sup>3</sup>DEPARTMENT OF ENVIRONMENT, TECHNOLOGY AND SOCIAL STUDIES, ROSKILDE UNIVERSITY, DK-4000, ROSKILDE, DENMARK

<sup>4</sup>LABORATOIRE DE GÉOLOGIE APPLIQUÉE, UNIVERSITÉ D'ANTANANARIVO, ANTANANARIVO, MADAGASCAR

RECEIVED JUNE 7, 2007; ACCEPTED MARCH 13, 2008  
ADVANCE ACCESS PUBLICATION APRIL 19, 2008

The 4000 km<sup>2</sup> Androy massif in southeastern Madagascar is a >2000 m thick sequence of interbedded basalt and rhyolite erupted during a widespread Cretaceous episode of predominantly basaltic volcanism. Two geochemically different groups of basalt, tholeiitic group B1 and mildly alkalic B2, are present, as are two different groups of rhyolite, R1 and R2. Both the basalts and rhyolites appear to have issued from relatively nearby feeders, as compositionally equivalent intrusions are exposed in the vicinity. The R2 rhyolites define a whole-rock Rb–Sr isochron of 84.0 ± 2.4 Ma (2σ), the same, within error, as an <sup>40</sup>Ar–<sup>39</sup>Ar sanidine age reported by earlier workers. Plate reconstructions suggest that the area was near the Marion hotspot at this time. Some involvement of hotspot mantle is allowed, but not required, by Nd–Pb–Sr isotope data for the basalts. The two types of basalt may have formed by different amounts of melting of the same mantle source, which remains rather poorly specified, but group B1 was affected much more than B2 by contamination with continental material, probably Archean crust. The R1 rhyolites are petrogenetically related to the B1 basalts, with which they are interbedded. The R2 rhyolites may be derived from melts of frozen high-ε<sub>Nd</sub> B1 basalt coupled with fractionation and assimilation of relatively small amounts of crust. Alternatively, although these rhyolites were erupted significantly later than the B2 basalts, they may have formed through advanced crystal fractionation of B2-type magma and relatively small amounts of crustal assimilation. Separate magmatic plumbing systems appear to have existed more or less contemporaneously in the Androy area.

KEY WORDS: large igneous province; rhyolite; mantle plume; basalt; Madagascar

## INTRODUCTION

Madagascar was the site of extensive basaltic volcanism between about 92 and 84 Ma, shortly before Madagascar and Greater India rifted apart (Storey *et al.*, 1995; Torsvik *et al.*, 1998). The volcanic episode is postulated to be linked to both rifting and the Marion (also known as Prince Edward) hotspot. Basalt flows along the southeastern coast of Madagascar had a source that was isotopically similar to those of recent volcanoes of the Marion and Crozet (≈500 km east of Marion) hotspots, but elsewhere geochemical evidence for a hotspot-type mantle source remains elusive (Mahoney *et al.*, 1991; Storey *et al.*, 1997; Melluso *et al.*, 2001, 2002). The amount of Cretaceous lava removed by erosion is uncertain, but most volcanic sections are less than 200 m thick today. By far the thickest remaining lava pile is in southeastern Madagascar at Volcan de l'Androy (Androy hereafter), where more than 2000 m of flows are present (Battistini, 1959) (Fig. 1a). The projected trends of three major dike swarms converge to the east of the Androy massif (Ernst & Buchan, 1997), and plate reconstructions and radiometric dating suggest that the Marion hotspot was centered near this area toward the

\*Corresponding author. Telephone: 1-808-956-8705.  
E-mail: jmahoney@hawaii.edu

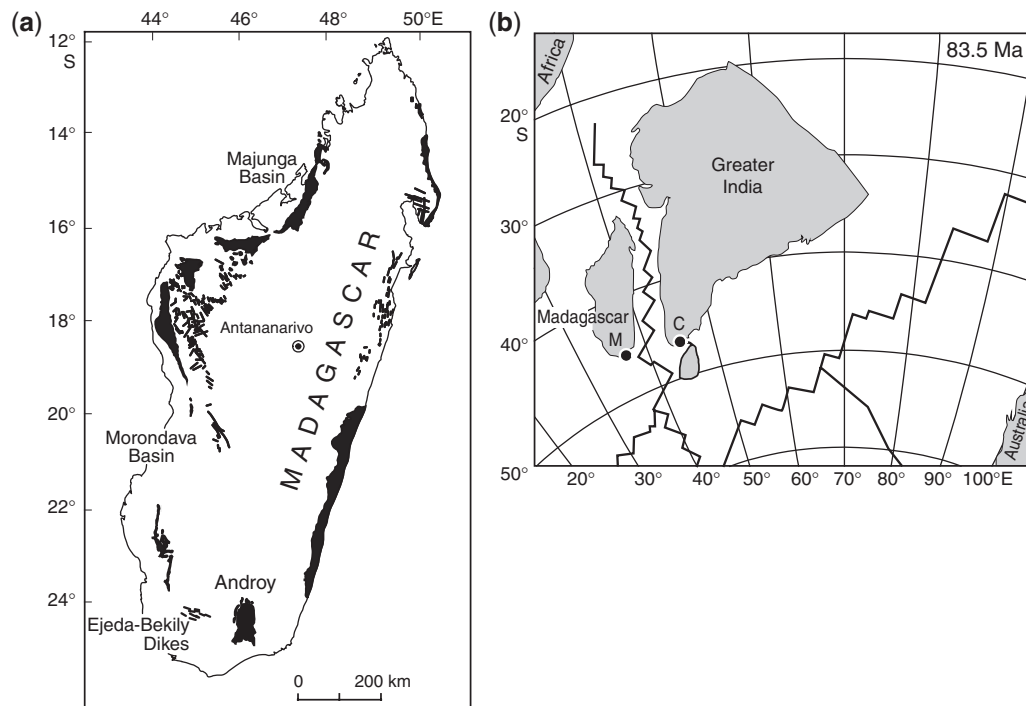


**Fig. 1.** (a) Principal outcrops of middle Cretaceous volcanic rocks in Madagascar, after Besairie (1964). (b) Plate reconstruction at 83.5 Ma (magnetic chron 34; from Kent *et al.*, 2002), shortly after the Androy eruptions. Locations of the Marion (M) and Crozet (C) hotspots assume these hotspots have remained stationary relative to the Earth's spin axis.

end of the magmatic episode (Fig. 1b) (e.g. Storey *et al.*, 1997; Kent *et al.*, 2002).

Apart from its great thickness and distinctive location, the Androy massif is unusual in that it is composed of interbedded basalt and abundant phenocryst-poor (generally <10% phenocrysts) rhyolite. Rhyolites are rare in most of the Madagascar province, although some are present along the central part of the rifted eastern margin and in the NW. Previous geochemical work has concentrated on the basalt-dominated flows and dikes along the eastern coast and in the Majunga and Morondava basins of western Madagascar (e.g. Mahoney *et al.*, 1991; Dostal *et al.*, 1992; Storey *et al.*, 1997; Melluso *et al.*, 1997, 2001, 2002, 2003; but see also Melluso *et al.*, 2005). In this study, we report major element, trace element, and Nd–Sr–Pb isotope data for the Androy massif, and investigate the relationships between the basaltic and silicic rocks.

Silicic rocks are also found in other large igneous provinces, although their abundance varies greatly. Both the Paraná–Etendeka and Karoo–Ferrar provinces are characterized by extensive rhyolite and trachydacite; however, silicic rocks are only minor components of the Deccan and Siberian Traps (e.g. see reviews in Macdougall, 1988). In the Columbia River province, silicic rocks were not erupted during the main Miocene phase of flood basalt formation, but are abundant, and in some intervals predominant, during subsequent development of the Snake River Plain and Yellowstone system (e.g. Doe *et al.*, 1982;

Hooper, 1997). Understanding the processes that lead to the formation of bimodal systems in some provinces but not in others is a major goal of studies of large igneous provinces, as is understanding of the interactions between mantle-derived melts and the crust.

## AGE AND FORM OF THE ANDROY MASSIF

Cretaceous volcanism began in northern Madagascar and migrated southward over a period of several million years. Storey *et al.* (1995) obtained an  $^{40}\text{Ar}–^{39}\text{Ar}$  age of  $84.4 \pm 1.0$  ( $2\sigma$ ) Ma for sanidine from a rhyolite (sample AND90-27) near the top of Vohitsimbe, the highest peak of the Androy massif. Plagioclase from a rhyolite dike (AND90-6) at the southeastern edge of the massif yielded an age of  $86.3 \pm 3.8$  Ma, and a dolerite (AND90-30) was dated at  $86.3 \pm 2.0$  Ma. Ages in the 84–86 Ma range also have been reported for basalt from the Ejeda–Bekily dike swarm to the west of Androy and, farther west, for lava flows of the southern Morondava Basin (Storey *et al.*, 1995; Torsvik *et al.*, 1998).

The Androy ('thorn forest') massif lies 100–150 km inland from the rifted eastern continental margin of Madagascar and forms a *c.* 4000 km<sup>2</sup> region of elevated topography. The overall structure is that of a large 'sag' caldera filled by a saucer-shaped pile of flows resting on Archean basement gneiss of the Androyen System



**Fig. 2.** Geological map of the Androy massif, modified after Battistini (1959) and Storey *et al.* (1997). Legend at lower right indicates the relationships between geochemical groups (see text) and the four volcanic series. Small numbers on axes are Madagascar National Survey grid system values; the latitude and longitude are also shown.

(Battistini, 1959; Storey *et al.*, 1997). The lowermost exposed flows are basalts, termed the Rim Series (Fig. 2), and are exposed best in the NE and NW. At least one rhyolite unit is present in the upper part of the Rim Series. The Rim Series is overlain by the inward-dipping Lower Rhyolites, which in many areas are also the lowest exposed flows in contact with basement. Above the Lower Rhyolites are gently inward-dipping basalt flows, the Main Series, interbedded with and overlain by rhyolites termed the Upper Rhyolites. Both the thickness of rhyolite units and the proportion of rhyolite to basalt increase toward the top of

the Main Series. The thickest units are 40–60 m thick, columnar-jointed rhyolites in the topmost portion of the Upper Rhyolites at Vohitsimbe. The Upper Rhyolites, in particular, lack eutaxitic textures (only one Androy silicic sample, AND90-18, shows any eutaxitic texture), suggesting that they may be lava flows rather than pyroclastic deposits, despite their high aspect ratio (generally >50:1).

The massif is flanked on the west and NE by additional outcrops of rhyolite and by intrusions of microgranite. Dikes of basalt and rhyolite crop out adjacent to the east and SE portions of the massif, and intrude some of the

Lower Rhyolites and Rim Series basalt flows. Textbook-type ring faults are not observed, although the microgranites and some of the dikes may represent intrusions that followed such faults. In comparison with the largest present-day basaltic–silicic central volcanic complexes, such as Torfajökull in Iceland (e.g. Gunnarsson *et al.*, 1998), the Androy complex is several times larger.

## SAMPLING AND ANALYTICAL METHODS

We collected samples from the massif and nearby dikes and microgranite intrusions (details of locations are given in Electronic Appendix 1, which is available for downloading at <http://www.petrology.oxfordjournals.org>). Good stratigraphic control is available for the ~900 m section of Main Series lavas and Upper Rhyolites at Vohitsimbe, where some 28 flows are exposed. Other flow samples were taken at lower stratigraphic levels, where exposure is more limited and stratigraphic position consequently is known only in a general way.

The methods used for bulk-rock chemical and Nd–Pb–Sr isotopic analysis were those of Storey *et al.* (1997). Concentrations of major elements and several trace elements were determined for all the samples by X-ray fluorescence spectrometry on agate-ground powders of amygdale- and vein-free chips of rock (Table 1; note that the oxides and totals are reported as volatile-free percentages). Additional trace elements were measured for a subset of powders by instrumental neutron activation analysis (Table 2). Isotope ratios of Nd, Sr, and Pb were measured for a smaller subset chosen to cover the range of major and trace element variation; corresponding parent and daughter element concentrations were determined by isotope dilution (Table 3). As in our past work, these concentrations are used principally for age-correcting isotope ratios; the isotope-dilution data do not necessarily represent bulk-rock values because small (~1 mm) hand-picked chips of rock were used for isotope analysis rather than bulk-rock powders (to avoid alteration and phenocrysts). Because the  $^{87}\text{Rb}/^{86}\text{Sr}$  ratios of most of the rhyolites are very high (as high as 113), the age-corrected  $(^{87}\text{Sr}/^{86}\text{Sr})_t$  values of the rhyolite samples are exceedingly sensitive to the choice of  $^{87}\text{Rb}$  decay constant and age [for example, for a  $^{87}\text{Rb}/^{86}\text{Sr}$  of 113, an age difference of 1 Myr leads to a difference in  $(^{87}\text{Sr}/^{86}\text{Sr})_t$  of 0.0016]. We use Storey *et al.*'s (1995) sanidine age of 84.4 Ma and, for the decay constant, Kossert's (2003) value of  $1.395 \times 10^{-11} \text{ year}^{-1}$ .

Mineral compositions were analyzed for a subset of samples chosen using the geochemical data and petrographical observations. Mineral analyses were obtained from polished thin sections with a JEOL JXA-8600S electron microprobe at the Department of Geology, University of Leicester, using an accelerating voltage of 15 kV and

a probe current of 30 nA with a beam diameter of 10  $\mu\text{m}$ . Count times of 20 s were used for measurement of characteristic peak intensities, with 10 s at each of the background positions selected on either side of the peak. Quantitative background-corrected results were standardized against a combination of synthetic materials and well-characterized natural minerals and corrected for matrix effects using a ZAF correction procedure. Minimum detection limits, calculated as three standard deviations above background, range from 0.02 wt % for  $\text{Na}_2\text{O}$  to 0.05 wt % for FeO and NiO. Olivines from thin sections of AND90-1 and AND90-7 were measured with a probe current of 100 nA and counting times of 80 s on both peak and (total) background for  $\text{TiO}_2$ ,  $\text{Al}_2\text{O}_3$  and NiO to improve the minimum detection limits for these oxides to 0.017, 0.008 and 0.013 wt %. The complete microprobe dataset is listed in Electronic Appendix 2.

## RESULTS

### Petrography and mineralogy

The samples have been subdivided into five types on the basis of whole-rock composition, particularly distinctive trace element characteristics (see below). We distinguish two groups of basalt, B1 and B2, and two groups of rhyolite (*sensu lato*), R1 and R2. Group R1 is divided further into subgroups R1a and R1b. Group R1a comprises mostly rhyolites, but also includes a small number of trachydacites and microgranites. The compositional differences are reflected in the mineralogy. B1 basalt samples are from flows of the Main Series and Upper Rhyolites and several dikes on the southeastern side of the massif. Group B2 rocks are much less abundant, at least in exposed parts of the massif. As flows, they are confined to the Rim Series, and thus lie stratigraphically below group B1 and the rhyolites. We also sampled a B2 dike on the northeastern side of the massif. Rhyolite group R1 is represented in both the Lower Rhyolites and Upper Rhyolites, and we sampled one R1 flow within a sequence of B2 basalts in the Rim Series. The microgranite intrusions and some of the dikes bordering the massif also belong to R1. In contrast, we found R2 rhyolites only in the Upper Rhyolites, interbedded with R1 rhyolites and B1 basalts. Lacroix (1923) reported an ankaratrite dike on the west side of Vohitsimbe, but we did not encounter such rocks.

### Group B1

Samples belonging to compositional group B1 range from aphyric to moderately porphyritic picrite and basalt, with up to 20% phenocrysts; they also include dolerite. Groundmass textures vary from hypocrystalline to holocrystalline and sub-ophitic; some samples show fluxion (flow) textures. Most of the B1 samples are sparsely porphyritic, with less than 10% phenocrysts. The main phenocryst assemblages are olivine (e.g. samples AND90-1, -7 and -13;

Table 1: X-ray fluorescence data

Sample		SiO <sub>2</sub>	TiO <sub>2</sub>	Al <sub>2</sub> O <sub>3</sub>	Fe <sub>2</sub> O <sub>3</sub> *	MnO	MgO	CaO	Na <sub>2</sub> O	K <sub>2</sub> O	P <sub>2</sub> O <sub>5</sub>	Total	LOI	Rb	Ba	Nb	Sr	Zr	Y	V	Cr	Ni
<i>Group B1</i>																						
AND90-1	dike	48.74	1.40	12.80	11.63	0.17	12.14	11.31	1.77	0.38	0.14	100.48	0.57	10	172	7	257	113	24	251	1010	305
AND90-2	dike	51.58	2.78	12.38	15.43	0.20	4.44	8.52	2.60	1.46	0.32	99.70	3.18	54	356	15	310	250	42	421	34	29
AND90-4	dike	54.79	2.68	12.53	13.76	0.18	3.08	6.60	2.89	2.68	0.48	99.66	1.78	100	595	22	318	352	57	165	2	8
AND90-5	dike	50.86	3.17	12.44	15.23	0.18	3.85	9.38	2.56	1.38	0.41	99.47	1.03	46	357	14	391	259	37	383	27	29
AND90-7		48.46	1.38	12.13	11.99	0.17	13.19	10.41	1.65	0.38	0.15	99.92	0.52	14	202	7	255	104	23	261	1360	382
AND90-8	dike	49.40	3.40	11.49	17.35	0.22	4.55	8.87	2.93	0.93	0.40	99.54	-0.45	34	465	15	335	291	51	464	43	38
AND90-9	dike	51.01	3.56	12.35	15.85	0.19	4.07	8.42	2.98	0.84	0.40	99.67	-0.29	46	407	22	422	354	54	369	29	38
AND90-12	dike	51.96	1.47	14.01	11.81	0.23	5.01	11.31	3.57	1.05	0.16	100.58	8.75	26	584	7	271	190	34	303	30	57
AND90-13		51.84	3.69	11.93	16.36	0.20	3.92	8.02	2.87	1.42	0.41	100.65	-0.36	62	410	21	283	359	55	381	18	30
AND90-19		57.99	2.00	12.63	13.69	0.12	1.83	5.68	1.93	3.85	1.00	100.72	5.54	82	858	35	249	436	64	97	b.d.	6
AND90-20	dike	56.90	1.96	12.36	14.20	0.15	1.91	6.06	1.67	3.41	0.97	99.59	5.21	66	926	33	285	436	66	92	b.d.	6
AND90-24		52.95	2.79	12.65	14.34	0.19	4.58	7.92	1.68	2.62	0.31	100.02	1.75	100	813	17	392	288	48	322	26	40
AND90-30		51.28	3.80	14.95	9.47	0.15	4.63	11.40	3.21	0.59	0.39	99.86	0.73	16	386	19	308	276	62	620	175	101
AND90-33		54.12	2.57	12.54	15.22	0.22	3.92	6.93	2.42	1.88	0.35	100.17	1.77	47	531	25	254	317	55	296	5	10
AND90-39		52.86	2.49	12.84	15.05	0.19	4.39	8.09	3.22	1.06	0.30	100.47	1.53	41	302	17	356	253	48	334	11	19
AND90-42a		51.64	2.64	12.73	18.09	0.20	3.41	6.39	4.41	0.17	0.32	99.99	5.88	9	79	20	150	280	87	403	11	22
AND90-42b		50.71	2.47	14.39	14.57	0.16	4.77	5.82	2.69	3.29	0.28	99.14	3.13	129	1088	18	384	249	44	376	46	28
AND90-44		52.65	2.21	12.97	13.74	0.17	5.05	9.34	2.67	1.01	0.26	100.07	0.48	24	365	15	294	227	44	313	27	25
AND90-46a		51.94	2.40	12.77	14.60	0.17	4.63	8.87	2.69	1.46	0.29	99.83	0.76	46	382	17	341	252	44	366	18	21
AND90-46b		50.98	1.86	14.71	11.99	0.16	5.59	9.07	2.88	1.20	0.21	98.65	2.24	33	405	11	372	205	32	268	42	45
AND90-47a		52.58	1.76	15.09	11.46	0.12	4.95	8.20	3.32	1.34	0.22	99.04	2.84	45	447	12	442	222	41	270	38	28
AND90-47b		53.26	2.70	11.92	14.85	0.21	3.30	8.09	2.14	2.51	0.31	99.29	5.38	146	595	15	350	240	40	379	31	32
AND90-49a		51.45	2.86	13.46	14.14	0.19	4.32	8.42	2.74	1.52	0.33	99.42	1.89	60	356	20	335	304	48	333	28	39
AND90-49b		53.26	2.85	12.81	14.46	0.18	4.51	8.70	2.59	1.01	0.32	100.70	1.53	35	325	20	337	304	47	340	30	39
AND90-49c		51.96	2.82	12.68	14.55	0.18	4.39	8.42	2.56	1.50	0.32	99.36	1.79	56	309	18	317	298	46	322	28	39
AND90-51		52.36	3.34	12.35	14.90	0.18	3.69	7.57	2.82	2.05	0.42	99.68	1.54	67	422	22	262	346	50	313	6	15
AND90-54	dike	52.78	1.68	14.05	11.60	0.15	5.53	10.51	2.15	0.56	0.19	99.20	4.05	25	517	9	791	179	29	269	74	47
AND90-55		54.62	2.23	13.70	10.11	0.14	3.76	9.82	4.34	0.32	0.27	99.33	7.50	13	218	12	305	216	33	274	62	44
AND90-56		52.85	2.35	14.31	11.88	0.14	4.08	10.09	3.12	0.31	0.27	99.39	2.95	10	286	15	400	230	35	298	71	48
AND90-57		52.23	2.30	14.30	12.44	0.17	5.32	9.89	2.00	1.08	0.26	99.98	2.32	43	274	13	456	222	34	284	82	51
AND90-58		51.89	2.24	14.17	11.89	0.15	5.32	9.85	2.65	0.68	0.26	99.09	1.78	34	299	14	440	216	34	255	58	58
AND90-59		54.04	2.53	12.24	15.56	0.19	4.13	8.43	2.39	1.37	0.33	101.21	1.55	41	414	20	299	271	45	383	14	15
AND90-60		50.12	3.32	13.28	15.20	0.19	4.54	8.09	2.78	1.20	0.41	99.12	0.29	36	379	15	367	269	38	377	35	30
AND90-62		57.37	2.09	12.51	13.18	0.14	3.43	5.12	2.36	2.79	0.25	99.25	4.13	71	810	12	216	277	45	356	12	13
AND90-64		49.07	4.20	12.39	16.60	0.18	4.04	6.32	3.77	2.93	0.49	99.98	1.78	103	618	24	474	425	66	300	23	64
AND90-65		51.86	3.02	13.01	15.00	0.17	4.36	7.01	3.98	1.41	0.33	100.15	1.62	35	293	18	193	291	45	364	16	26
AND90-68		51.05	2.51	13.28	14.32	0.20	5.49	9.19	2.79	1.13	0.27	100.22	0.18	35	277	13	287	231	37	315	37	45
<i>Group B2</i>																						
AND90-14		48.35	3.64	14.06	14.44	0.16	3.55	10.07	2.41	1.25	0.51	98.44	6.82	19	411	31	495	293	41	288	15	35
AND90-73		47.54	3.50	14.24	14.84	0.19	5.87	9.08	3.20	1.40	0.42	100.28	1.98	27	561	40	960	238	36	329	52	74
AND90-74	dike	47.84	3.77	13.37	14.62	0.19	5.49	9.13	2.20	2.17	0.38	99.16	2.44	50	771	33	789	265	31	364	44	42
AND90-75		46.92	3.50	12.43	15.90	0.21	6.37	9.89	2.21	1.66	0.43	99.53	2.81	39	333	38	851	240	36	333	57	89
AND90-76		47.85	3.48	12.80	14.50	0.20	5.06	10.66	2.34	1.81	0.42	99.12	2.14	40	427	40	917	240	33	335	67	74
AND90-77		48.12	3.37	14.61	14.16	0.14	5.95	9.06	2.45	1.22	0.37	99.45	2.43	23	554	30	757	216	40	310	50	73

(continued)

Table 1: Continued

Sample	SiO <sub>2</sub>	TiO <sub>2</sub>	Al <sub>2</sub> O <sub>3</sub>	Fe <sub>2</sub> O <sub>3</sub> *	MnO	MgO	CaO	Na <sub>2</sub> O	K <sub>2</sub> O	P <sub>2</sub> O <sub>5</sub>	Total	LOI	Rb	Ba	Nb	Sr	Zr	Y	V	Cr	Ni	
AND90-78	49.81	2.70	13.41	12.99	0.18	6.70	9.59	2.73	1.37	0.35	99.83	1.05	27	373	34	619	234	31	278	97	51	
AND90-79	50.65	2.68	13.13	12.78	0.17	6.55	9.73	2.53	1.32	0.34	99.87	0.66	20	364	35	554	240	32	295	100	50	
AND90-80	48.47	4.19	11.86	16.69	0.21	4.48	8.60	2.99	2.15	0.65	100.30	2.51	43	563	72	561	382	67	333	10	27	
AND90-82	48.54	3.30	13.73	14.57	0.16	5.79	9.88	2.39	1.34	0.39	100.10	0.24	35	607	52	758	248	40	346	105	95	
<i>Group R1a</i>																						
AND90-6	dike	76.09	0.53	11.01	2.38	0.08	0.32	1.24	2.94	4.83	0.06	99.47	0.97	162	994	29	149	549	60	1	b.d.	3
AND90-10	dike	78.21	0.27	11.32	2.31	0.01	0.28	0.28	1.79	4.95	0.04	99.45	1.75	143	1435	38	55	591	66	6	b.d.	4
AND90-11		72.64	0.58	11.61	4.19	0.07	0.34	2.33	2.23	5.25	0.07	99.30	3.31	146	948	37	102	431	77	49	5	8
AND90-16		77.51	0.71	11.17	4.09	0.03	0.40	0.31	1.87	4.69	0.10	100.88	1.91	165	2336	27	129	505	58	1	2	3
AND90-17		77.58	0.62	11.26	2.25	0.02	0.37	0.23	1.71	4.94	0.06	99.03	1.30	182	967	29	95	556	65	b.d.	b.d.	3
AND90-18		66.28	0.48	14.82	6.94	0.09	0.31	0.41	2.46	7.65	0.06	99.51	1.14	202	741	67	85	1598	103	b.d.	b.d.	4
AND90-21		77.13	0.60	10.88	2.32	0.02	0.37	0.85	2.03	4.85	0.06	99.10	2.09	174	2661	28	199	517	73	b.d.	b.d.	3
AND90-22	clast	66.29	0.74	13.35	7.36	0.14	0.48	2.71	2.82	5.57	0.18	99.64	2.64	166	1333	56	179	826	84	b.d.	b.d.	4
AND90-23		65.00	0.94	12.99	9.09	0.16	0.69	3.61	2.92	4.85	0.30	100.55	2.95	136	1410	48	264	697	80	4	b.d.	4
AND90-32		77.11	0.23	11.11	2.36	0.01	0.09	b.d.	2.33	5.77	0.03	99.04	1.20	215	106	62	3	634	81	b.d.	b.d.	3
AND90-48		78.73	0.21	10.69	2.32	0.03	0.24	0.22	2.32	4.99	0.01	99.77	0.97	164	174	56	18	592	114	4	b.d.	4
AND90-61		76.21	0.38	12.26	2.61	0.03	0.54	0.10	0.59	6.50	0.03	99.25	2.04	195	1086	39	64	613	59	b.d.	13	3
AND90-66		77.70	0.21	11.01	2.50	0.07	0.09	0.32	2.83	5.77	0.01	100.50	0.81	210	102	58	13	598	125	b.d.	1	3
AND90-69		73.19	0.59	12.33	4.21	0.08	0.43	0.57	4.01	4.88	0.12	100.40	1.28	167	1014	35	153	630	157	b.d.	b.d.	4
AND90-70		71.38	0.58	12.02	4.84	0.11	0.46	2.31	3.35	4.05	0.09	99.18	1.01	145	798	36	366	647	74	b.d.	b.d.	3
AND90-71		71.89	0.58	12.26	4.33	0.09	0.48	1.51	4.63	4.46	0.09	100.32	0.95	150	832	36	216	633	75	b.d.	b.d.	3
AND90-72		70.58	0.63	12.03	5.95	0.14	0.43	2.36	3.97	3.68	0.11	99.87	0.31	121	760	39	239	700	83	b.d.	b.d.	3
AND90-81	mgr	74.46	0.60	11.77	2.82	0.10	0.26	1.34	3.52	4.81	0.06	99.74	1.04	166	907	30	175	518	58	b.d.	1	3
AND90-83		76.48	0.53	11.02	2.20	0.09	0.31	1.02	3.15	4.94	0.05	99.79	0.22	190	1030	30	168	526	54	1	1	3
<i>Group R1b</i>																						
AND90-25		78.98	0.18	10.80	1.55	0.01	0.12	b.d.	3.14	5.32	0.01	100.11	0.56	207	52	60	3	495	66	b.d.	b.d.	2
AND90-26		80.84	0.16	9.77	1.12	0.01	0.10	b.d.	2.70	4.89	0.02	99.62	0.93	186	48	54	4	442	40	b.d.	3	2
AND90-27		79.14	0.18	10.57	1.80	0.01	0.16	0.12	2.90	5.37	0.02	100.27	0.83	210	60	59	6	498	111	b.d.	2	3
AND90-28		77.86	0.17	10.72	2.55	0.02	0.13	0.14	2.83	6.01	0.04	100.48	0.74	208	68	61	8	503	95	b.d.	b.d.	3
AND90-29		78.69	0.20	10.05	1.42	0.01	0.12	b.d.	2.60	5.52	0.02	98.63	0.44	193	157	55	5	547	92	b.d.	b.d.	2
AND90-31		77.80	0.22	11.05	1.60	0.01	0.11	0.17	2.97	5.47	0.02	99.41	0.62	204	104	57	5	592	91	1	1	3
AND90-37		76.90	0.23	10.80	2.63	0.02	0.30	0.14	2.63	5.54	0.02	99.21	0.81	201	233	53	10	624	72	8	8	5
AND90-38		78.87	0.23	10.28	2.32	0.01	0.18	b.d.	3.41	4.95	0.02	100.28	0.57	177	127	52	4	607	75	2	b.d.	2
AND90-45		78.64	0.19	11.12	1.06	0.04	0.46	0.46	1.15	5.94	0.03	99.08	2.54	195	145	62	38	533	104	5	b.d.	4
AND90-50		79.33	0.08	11.25	1.55	0.01	0.34	0.22	4.09	4.07	0.02	100.97	1.51	284	86	105	23	311	108	6	b.d.	3
<i>Group R2</i>																						
AND90-34		73.95	0.41	12.39	4.64	0.02	0.35	0.28	2.97	4.55	0.03	99.60	1.80	268	42	208	77	1436	179	2	b.d.	3
AND90-35		70.69	0.45	12.75	4.86	0.11	0.00	0.16	5.06	5.10	0.02	99.19	0.70	243	10	201	11	1332	139	4	b.d.	3
AND90-36		72.63	0.37	11.92	5.60	0.13	0.17	0.20	5.67	3.94	0.03	100.65	0.49	184	16	210	4	1382	170	b.d.	b.d.	4
AND90-40		76.28	0.36	11.65	2.96	0.02	0.35	0.18	3.93	3.92	0.02	99.68	1.38	318	142	186	25	1132	135	7	b.d.	4
AND90-41		75.06	0.38	12.07	2.94	0.02	0.19	0.14	4.20	4.02	0.01	99.04	0.87	207	53	201	28	1488	171	5	1	4
AND90-43		72.40	0.40	12.32	5.44	0.12	0.13	0.35	7.07	2.50	0.03	100.77	0.18	121	9	182	21	1282	147	9	1	3
AND90-52		73.18	0.40	12.12	5.78	0.06	0.18	0.13	4.52	4.27	0.06	100.69	1.07	209	80	190	11	1434	193	12	b.d.	6
AND90-53		73.73	0.36	11.37	5.24	0.13	0.17	0.41	5.49	4.41	0.02	101.35	0.43	249	88	215	8	1600	157	4	b.d.	4

(continued)

Table 1: Continued

Sample	SiO <sub>2</sub>	TiO <sub>2</sub>	Al <sub>2</sub> O <sub>3</sub>	Fe <sub>2</sub> O <sub>3</sub> *	MnO	MgO	CaO	Na <sub>2</sub> O	K <sub>2</sub> O	P <sub>2</sub> O <sub>5</sub>	Total	LOI	Rb	Ba	Nb	Sr	Zr	Y	V	Cr	Ni
<i>Standards</i>																					
<i>Basalts W-1, W-2</i>																					
Measured	52.57	1.10	15.16	11.19	0.17	6.61	11.09	2.40	0.61	0.14	101.05		23	185	6	198	99	22	257	92	71
Compiled	52.50	1.07	15.01	11.12	0.17	6.62	10.99	2.16	0.64	0.13	100.41		21	176	7.8	193	97	23	261	92	70
<i>Granite NIM-G</i>																					
Measured	76.26	0.11	12.15	2.00	0.02	b.d.	0.76	3.84	5.02	0.01	100.14		316	115	54	12	302	143	b.d.	19	12
Compiled	75.88	0.09	12.08	2.02	0.02	0.06	0.78	3.36	4.99	0.01	99.29		320	120	53	10	300	143	2	12	8

Major element oxides, totals, and LOI (weight loss on ignition to 950°C for 24 h) are in wt %. Oxides and totals are volatile-free values. Trace element concentrations are in ppm. Fe<sub>2</sub>O<sub>3</sub>\* is total iron as Fe<sub>2</sub>O<sub>3</sub>. Unless otherwise indicated, samples are from flows; mgr, microgranite intrusion; clast, a clast from a rhyolitic breccia. Relative precision is 0.5% for SiO<sub>2</sub>, 1% for other major elements, and ~5% for trace elements; b.d., below detection limit. Measured values for standards W-1 (for major elements;  $n=5$ ), W-2 (for trace elements;  $n=5$ ) and NIM-G (for both;  $n=3$ ) run as unknowns are compared with recommended (compiled) values (GeoReM, 2006; see <http://georem.mpch-mainz.gwdg.de/start.asp>). Measurements were made at the University of Leicester [see Storey *et al.* (1997) for details].

these also contain rare pyroxene phenocrysts), plagioclase (AND90-42b), plagioclase + olivine (AND90-8), plagioclase + augite (AND90-51, -56, -57), and olivine + plagioclase + augite (AND90-47A). In many samples, the pyroxene occurs with plagioclase in glomerocrysts. Magnetite or titanomagnetite phenocrysts are present in several samples, and magnesiochromite is embedded in olivine in AND90-7. Alteration in the B1 samples ranges from slight to severe, as reflected crudely by variable whole-rock weight loss on ignition (LOI, -0.45 to 8.75 wt %). The development of calcite in the groundmass is common, and green or brown clay sometimes replaces glassy mesostasis. Some B1 basalts are amygdale-rich, with fillings of calcite, quartz and chlorite.

The main silicate and oxide phases in four B1 samples (AND90-1, -7, -13 and -57) were analyzed by electron microprobe. Unaltered olivine phenocrysts in samples AND90-1 and -7 have high forsterite (Fo) contents. Sample AND90-7 contains the most magnesian olivine, with several crystals exceeding Fo<sub>91</sub> [maximum Fo<sub>91.8</sub> (core) ranging to Fo<sub>86.2</sub> (rim)]. The CaO content of these phenocrysts is between 0.2 and 0.3 wt %. Nickel oxide mostly ranges from 0.2 to 0.4 wt %, typical of basaltic olivine; however, a few phenocrysts contain more than 0.6 wt % NiO, higher than the most nickel-rich olivine in Hawaiian shield basalts (Sobolev *et al.*, 2005). The crystals are anhedral to subhedral, with textures suggesting fragmentation, but none shows indications of the strain shadows often found in xenocrysts. Small olivine phenocrysts in AND90-13, a ferrobasalt, are more iron-rich (Fo<sub>32-34</sub>). No olivine was found in sample AND90-57.

Groundmass and microphenocryst plagioclase is in the range of An<sub>65-75</sub> in AND90-1 and AND90-7, An<sub>51-59</sub> in AND90-13, and An<sub>64-70</sub> in AND90-57 (Fig. 3a).

Pyroxene compositions vary from Ca<sub>46</sub>Mg<sub>46</sub>Fe<sub>8</sub> to Ca<sub>36</sub>Mg<sub>36</sub>Fe<sub>28</sub>; that is, from diopside (AND90-1) to augite (AND90-7, -13, and -57; see Fig. 4). Many grains exhibit slight normal crystal zoning. No low-calcium pyroxene was found in the B1 samples.

#### Group B2

All the B2 basalts are porphyritic, with up to 25% phenocrysts. The dominant phenocryst assemblages are augite (AND90-79), augite + plagioclase (AND90-75, -76, -78), plagioclase + magnetite (AND90-14), and plagioclase (AND90-73). No olivine was found, reflecting the absence of any near-primitive bulk-rock compositions within this group (see below). Groundmass textures range from hypocrystalline to holocrystalline, sub-ophitic. As with group B1, alteration varies from slight to severe. Green or brown clay sometimes replaces glassy mesostasis. Secondary calcite is scarce. A few samples contain clay- and epidote-filled vesicles (AND90-80, -82) but most samples are amygdale- and vesicle-free. Overall, the B2 samples tend to be somewhat less altered than the B1 samples.

Pyroxene crystals in sample AND90-78 were analyzed by electron microprobe. All are augite, ranging from Ca<sub>43</sub>Mg<sub>47</sub>Fe<sub>10</sub> to Ca<sub>37</sub>Mg<sub>46</sub>Fe<sub>17</sub> (Fig. 4). This slight variation reflects core-to-rim zonation. No feldspars of group B2 were analyzed.

#### Group R1a

Group R1a is composed predominantly of rhyolite but also includes three samples of trachydacite (AND90-18, -22, and -23). The rocks vary from aphyric to moderately phyrific, with up to 20% phenocrysts; most samples contain ~10% phenocrysts. Plagioclase feldspar is a common phenocryst phase. In some samples, it is accompanied by

Table 2: Neutron activation data

Sample	Sc	Co	La	Ce	Nd	Sm	Eu	Gd	Tb	Yb	Lu	Ta	Hf	Th
<i>Group B1</i>														
AND90-1	34	59	10.1	23.4	14.5	3.77	1.27	4.13	0.79	2.06	0.30	0.45	2.82	1.20
AND90-2	29	47	27.3	59.9	32.4	7.28	2.20	7.50	1.20	3.28	0.47	0.99	5.86	7.30
AND90-4	21	b.d.	42.4	92.5	48.8	10.5	2.69	10.1	1.68	4.30	0.63	1.55	8.34	8.48
AND90-7	35	67	9.50	23.0	14.3	3.54	1.27	4.36	0.76	1.93	0.28	0.41	2.58	1.04
AND90-8	37	51	26.6	61.5	37.6	8.94	2.95	9.67	1.69	4.03	0.60	0.99	6.99	2.81
AND90-13	31	47	33.0	73.1	41.0	9.72	3.00	10.5	1.79	4.23	0.63	1.33	8.53	5.45
AND90-20	16	25	54.5	112	56.8	12.5	4.02	12.5	2.06	4.67	0.68	1.91	9.27	6.32
AND90-24	27	44	29.8	63.3	35.0	8.29	2.48	8.33	1.59	3.69	0.51	1.18	6.98	6.10
AND90-33	30	44	41.7	87.2	42.8	9.10	2.64	9.48	1.48	4.40	0.67	1.45	7.67	6.59
AND90-39	34	48	32.0	65.5	34.6	7.36	2.37	7.58	1.31	3.80	0.56	1.18	6.27	4.68
AND90-42a	33	50	47.1	67.6	42.3	9.41	2.75		1.68	3.93	0.56	1.12	6.35	4.79
AND90-42b	38	52	28.6	59.4	30.1	7.30	2.23	7.14	1.10	3.37	0.48	1.05	5.91	4.22
AND90-46a	33	48	29.1	61.8	32.8	7.51	2.35	8.35	1.33	3.85	0.56	1.08	6.21	4.48
AND90-49b	27	49	30.6	63.9	36.1	8.36	2.47	8.23	1.62	3.66	0.51	1.20	7.02	6.25
AND90-51	29	45	35.5	77.7	41.9	9.31	2.72	9.56	1.40	3.95	0.57	1.42	8.07	6.73
AND90-54	27	43	22.7	45.9	22.8	5.00	1.65	4.90	0.83	2.37	0.36	0.56	4.55	3.47
AND90-58	26	42	23.6	51.8	30.2	6.78	2.00	7.23	1.06	2.78	0.38	0.96	5.37	4.43
AND90-60	29	47	29.6	66.8	36.6	8.17	2.56	8.64	1.17	2.96	0.42	1.06	6.70	6.30
AND90-64	25	51	44.1	95.7	55.7	12.9	3.57	12.8	1.96	4.86	0.69	1.71	10.4	7.61
<i>Group B2</i>														
AND90-75	27	54	42.1	90.8	45.6	9.13	2.86	8.42	1.21	2.59	0.37	2.57	6.41	4.98
AND90-76	28	54	42.0	89.5	43.5	8.62	2.93	8.35	1.48	2.66	0.37	2.57	6.43	5.04
AND90-78	26	51	38.9	80.4	37.7	7.64	2.42	6.86	1.03	2.54	0.36	2.07	5.87	4.96
AND90-82	29	58	54.4	101	48.8	9.41	2.96	8.57	1.54	2.78	0.39	3.10	6.17	5.61
<i>Group R1a</i>														
AND90-6	7.3	0.9	79.9	158	70.2	12.8	2.59	10.8	1.66	4.98	0.66	1.83	13.9	25.3
AND90-17	8.0	b.d.	94.7	177	79.5	14.7	2.93	12.3	1.63	4.82	0.63	1.73	13.3	25.6
AND90-18	8.0	b.d.	206	352	177	31.5	7.29	25.8	3.71	7.61	1.07	3.88	31.4	17.2
AND90-23	13	6.2	88.7	188	88.4	16.8	4.84	15.6	2.48	6.22	0.88	2.94	15.9	16.3
AND90-32	0.6	b.d.	169	86.2	104	16.9	0.95	14.3	1.87	9.13	1.29	4.14	19.9	26.6
AND90-48	0.4	b.d.	87.5	197	91.0	19.1	1.07	19.8	2.91	10.2	1.41	3.67	17.8	23.1
AND90-61	6.0	b.d.	96.7	75.3	80.6	14.2	2.67	13.5	1.56	5.78	0.82	2.36	16.0	24.6
AND90-71	9.2	b.d.	71.7	151	74.8	15.3	3.45	15.0	1.98	6.19	0.86	2.18	15.5	19.6
AND90-72	10	b.d.	69.9	153	79.0	16.7	3.95	16.8	2.34	7.23	1.01	2.52	17.9	18.1
AND90-83	7.2	b.d.	79.9	159	70.5	13.0	2.50	14.3	1.52	4.93	0.68	1.84	13.3	25.1
<i>Group R1b</i>														
AND90-25	0.5	1.6	13.8	26.0	14.8	3.84	0.45	4.55	1.36	8.05	1.11	3.90	16.9	14.9
AND90-27	0.5	b.d.	27.5	66.2	34.5	9.30	0.58	11.1	2.24	12.2	1.70	4.04	16.2	22.2
AND90-29	0.5	b.d.	38.9	95.0	47.4	10.9	0.88	13.5	1.89	9.20	1.35	3.48	16.7	21.0
AND90-31	0.4	b.d.	13.6	34.4	16.3	4.33	0.47	6.23	1.28	10.1	1.44	3.82	18.5	16.6
AND90-37	0.8	2.4	39.5	53.8	48.4	10.8	0.75	11.4	1.67	8.32	1.16	3.76	18.9	22.7
AND90-50	0.3	2.4	33.5	69.0	28.5	7.35	0.21		1.48	11.9	1.66	7.97	15.8	33.2

(continued)

Table 2: Continued

Sample	Sc	Co	La	Ce	Nd	Sm	Eu	Gd	Tb	Yb	Lu	Ta	Hf	Th
<i>Group R2</i>														
AND90-34	0.6	b.d.	80.4	142	72.7	19.9	1.41	22.8	4.01	16.6	2.33	11.7	30.3	42.2
AND90-41	0.7	b.d.	58.0	94.4	54.5	13.8	0.96	20.5	3.15	17.2	2.46	13.3	33.9	48.9
AND90-43	0.6	b.d.	92.4	193	75.3	14.9	1.07	20.1	2.95	15.2	2.19	10.6	27.2	36.6
AND90-53	0.5	2.9	69.2	162	63.3	14.5	1.15	22.4	2.60	16.8	2.41	13.2	34.9	54.0
<i>Standard</i>														
JB-1A														
Measured	29	39.5	38.1	66.2	26.7	5.38	1.59	4.95	0.68	2.21	0.30	1.67	3.79	9.75
Compiled	27.9	39	37.8	66	25.7	5.07	1.47	4.6	0.69	2.1	0.33	1.97	3.46	8.9

Concentrations are in ppm; b.d., below detection limit. Relative precision is ~10%. An indication of accuracy is given by comparison of compiled (GeoReM, 2006; see <http://georem.mpch-mainz.gwdg.de/start.asp>) and measured ( $n=5$ ) values of standard JB-1 run as an unknown. Measurements were made at the University of Leicester [see Storey *et al.* (1997) for details].

quartz, ilmenite, magnetite, accessory zircon, and, rarely, sanidine. Pyroxene occurs in several samples. The groundmass, which in some samples shows devitrification textures, comprises mostly feldspar and quartz,  $\pm$  magnetite. Only one sample (AND90-18) exhibits any eutaxitic texture. Sample AND90-22 is a porphyritic granophyre, with spectacular graphic intergrowths of quartz and alkali feldspar, phenocrysts of quartz and albite, and trace amounts of an altered mafic mineral, possibly originally amphibole. AND90-72 and -81 are samples of two-feldspar (subsolvus) microgranite from the NE quadrant of the Androy massif. They exhibit strong granophyric textures, and contain hedenbergite. Accessory zircon and apatite are also present in these samples. All of the R1a samples are altered; the alteration ranges from minor iron staining and slight alteration of feldspars and mesostasis to complete replacement of feldspars and mesostasis by clay, zeolite, quartz, and calcite. Pyroxene in microgranite AND90-72 is partially replaced by a pale olive-green amphibole, ferroedenite.

The main silicate phases in three samples of rhyolite (AND90-48, -71, -83), a trachydacite (AND90-23), and microgranite (AND90-72) from group R1a were analyzed by electron microprobe. Plagioclase in AND90-23, -72 and -83 is predominantly andesine or oligoclase (Fig. 3b); in addition, alkali feldspar crystals were found in AND90-72 and -23. The feldspar in rhyolite AND90-48 comprises large, euhedral, but slightly rounded phenocrysts of perthitic feldspar. One set of lamellae is pure albite, but we were unable to analyze the other (presumably orthoclase) lamellae. AND90-71, -72 and -83 contain clinopyroxene. The crystals in AND90-71 are 0.1–0.4 mm across, subhedral, and comprise both augite and pigeonite (Fig. 4). Using the microprobe's electron backscatter facility, it is possible to distinguish the Ca-rich, Fe-poor (dark) and

Ca-poor, Fe-rich (light) components. The low-Ca pyroxenes tend to rim the Ca-rich ones. The pyroxene phenocrysts in microgranite AND90-72 are anhedral, dark green hedenbergite, whereas those in rhyolite AND90-83 are partially rounded and resorbed augite, with Fs/En (ferrosilite/enstatite) ratios that are low for rhyolites; they may be xenocrystic. The pyroxene pairs in rhyolite AND90-71 indicate low temperatures of equilibration (very roughly 800–850°C), and the high Ca content of the hedenbergite in microgranite AND90-72 is consistent with the subsolvus textures and equilibration at a temperature of about 600°C (Lindsley & Andersen, 1983).

#### Group R1b

These high-silica rhyolites were collected from the Vohitsimbe massif. All are porphyritic, with between 20 and 25% phenocrysts comprising alkali feldspar (sanidine or perthite), quartz, and minor magnetite. No plagioclase, pyroxene, or amphibole was seen, although accessory zircon was found in several samples. The groundmass is usually a devitrified assemblage of quartz, feldspar, and magnetite, but in some samples it is cryptocrystalline or vitreous (e.g. AND90-28). AND90-50 is a crystal tuff. Only one R1b sample (AND90-25) exhibits any flow banding and none show eutaxitic textures. Alteration is less than in the R1a rhyolites; feldspars are nearly fresh, and a slight oxidation and development of pale brown clay in the groundmass is the main sign of alteration.

The main silicate phases in four R1b samples (AND90-26, -28, -37 and -45) were analyzed by electron microprobe. Sanidine ( $\sim\text{An}_2\text{Ab}_{48}\text{Or}_{50}$ ) occurs in AND90-26 and -28, whereas AND90-37 and -45 contain partially resorbed and embayed perthite phenocrysts with almost pure end-member Na- and K- feldspar segregations (Fig. 3c).

Table 3: Isotope ratios and parent–daughter element concentrations

Sample:	AND90-1(d)	AND90-8(d)	AND90-24	AND90-33	AND90-39	AND90-46a	AND90-49b	AND90-54(d)	AND90-64	AND90-76	AND90-78	AND90-82
Group:	B1	B1	B1	B1	B1	B1	B1	B1	B1	B2	B2	B2
$\epsilon_{Nd}(0)$	-3.6	-2.9	-7.6	-11.1	-7.1	-7.5	-7.6	-13.8	-7.8	-0.2	-3.3	-0.4
$(^{143}Nd/^{144}Nd)_m$	0.512458	0.512493	0.512249	0.512070	0.512278	0.512258	0.512249	0.511931	0.512240	0.512630	0.512473	0.512621
$(^{87}Sr/^{86}Sr)_m$	0.70923	0.71063	0.71250	0.71529	0.71202	0.71204	0.71218	0.71515	0.71370	0.70641	0.70747	0.70595
$(^{206}Pb/^{204}Pb)_m$	19.014	18.157	18.930	18.651	18.741	18.706	18.898	18.695	18.562	18.726	18.293	18.836
$(^{207}Pb/^{204}Pb)_m$	15.850	15.872	15.850	15.919	15.962	15.946	15.850	15.925	15.823	15.672	15.691	15.713
$(^{208}Pb/^{204}Pb)_m$	40.055	39.526	40.741	40.734	41.023	40.730	40.684	40.696	40.644	39.656	39.955	39.783
<i>ppm</i>												
Nd	9.609	22.17	36.45	20.06	17.83	19.65	36.1	21.66	31.24	43.5	38.58	48.8
Sm	2.687	5.777	8.399	4.404	4.228	4.896	8.36	4.853	7.409	8.62	7.665	9.41
Sr	251.9	323.6	391.2	285.8	348.1	370.6	335.2	538.7	517.2	917	634.5	758
Rb	5.78	36.4	91.6	44.3	35.6	50.3	59.5	24.0	70.2	40	25.1	35
Pb	0.9050	2.535	4.118	3.987	2.332	2.364	4.844	2.053	5.451	4.356	5.303	5.681
U	0.186	0.384	0.467	0.505	0.275	0.291	0.587	0.195	0.712	0.634	0.565	1.034
Th	0.812	2.28	3.70	3.58	2.09	2.12	4.35	1.84	4.89	3.91	3.75	5.10
$\epsilon_{Nd}(t)$	-3.2	-2.4	-7.0	-10.4	-6.5	-6.9	-7.0	-13.2	-7.2	0.6	-2.4	0.5
$(^{143}Nd/^{144}Nd)_t$	0.512365	0.512406	0.512172	0.511997	0.512199	0.512175	0.512172	0.511856	0.512161	0.512564	0.512407	0.512557
$(^{87}Sr/^{86}Sr)_t$	0.70915	0.71025	0.71171	0.71476	0.71167	0.71158	0.71158	0.71500	0.71324	0.70626	0.70734	0.70579
$(^{206}Pb/^{204}Pb)_t$	18.915	18.088	18.861	18.589	18.708	18.665	18.833	18.663	18.503	18.545	18.202	18.632
$(^{207}Pb/^{204}Pb)_t$	15.845	15.869	15.847	15.916	15.960	15.944	15.847	15.923	15.820	15.663	15.687	15.703
$(^{208}Pb/^{204}Pb)_t$	39.913	39.391	40.562	40.590	40.940	40.633	40.526	40.596	40.510	39.289	39.757	39.452
Sample:	AND90-6(d)	AND90-18	AND90-23	AND90-27	AND90-29	AND90-34	AND90-41	AND90-43	AND90-48	AND90-53	AND90-83	
Group:	R1a	R1a	R1a	R1b	R1b	R2	R2	R2	R1a	R2	R1a	
$\epsilon_{Nd}(0)$	-17.9	-10.4	-12.5	-8.2	-8.2	-2.8	-2.6	-3.3	-8.3	-3.2	-18.2	
$(^{143}Nd/^{144}Nd)_m$	0.511723	0.512106	0.512001	0.512222	0.512220	0.512498	0.512508	0.512473	0.512216	0.512478	0.511707	
$(^{87}Sr/^{86}Sr)_m$	0.73990	0.72547	0.72175	0.84103	0.84552	0.72478	0.73850	0.73520	0.76113	0.80142	0.73993	
$(^{206}Pb/^{204}Pb)_m$	18.562	18.653	18.284	18.886	18.871	18.861	18.910	18.900	18.872	18.949	18.588	
$(^{207}Pb/^{204}Pb)_m$	15.868	15.865	15.774	15.895	15.875	15.824	15.817	15.815	15.883	15.836	15.833	
$(^{208}Pb/^{204}Pb)_m$	41.628	40.358	40.766	40.808	40.686	40.462	40.400	40.400	40.757	40.380	41.440	
<i>ppm</i>												
Nd	70.2	132.33	75.54	43.22	44.98	72.75	59.24	58.43	70.62	56.79	67.7	
Sm	12.83	21.64	14.41	11.83	10.66	19.82	13.99	12.27	14.78	13.52	12.32	
Sr	149.4	84.93	207.0	5.989	5.012	77.80	26.64	14.64	13.03	9.456	165.3	
Rb	162	205.5	144.6	229.8	195.5	260.1	198.8	95.00	187.7	243.4	189.8	
Pb	28.18	27.61	24.30	27.74	21.36	46.98	52.81	38.18	23.54	60.89	24.36	
U	1.53	1.51	1.12	3.32	1.71	5.33	8.31	5.45	3.26	7.49	1.01	
Th	25.3	17.2	16.3	18.1	19.2	42.2	47.4	34.3	23.1	54.7	21.9	
$\epsilon_{Nd}(t)$	-17.0	-9.4	-11.6	-7.8	-7.6	-2.4	-2.0	-2.5	-7.5	-2.6	-17.3	
$(^{143}Nd/^{144}Nd)_t$	0.511662	0.512051	0.511937	0.512131	0.512141	0.512407	0.512429	0.512403	0.512146	0.512399	0.511646	
$(^{87}Sr/^{86}Sr)_t$	0.73622	0.71724	0.71938	0.71069	0.71303	0.71342	0.71308	0.71382	0.71201	0.71322	0.73602	
$(^{206}Pb/^{204}Pb)_t$	18.517	18.606	18.244	18.782	18.803	18.649	18.612	18.708	18.751	18.699	18.553	
$(^{207}Pb/^{204}Pb)_t$	15.866	15.863	15.772	15.890	15.872	15.814	15.803	15.806	15.877	15.824	15.831	
$(^{208}Pb/^{204}Pb)_t$	41.385	40.181	40.576	40.621	40.437	39.912	39.843	40.004	40.476	39.781	41.193	

Measured (subscript m) isotope ratios are age-corrected (subscript t) to 84.4 Ma. Dike samples are indicated by (d). Isotope ratios are reported relative to 0.511850 for La Jolla Nd, to 0.71024 for NBS 987 Sr, and to the NBS 981 Pb values of Todt *et al.* (1996). Reproducibility for NBS 987 Sr over a 3 year period was  $\pm 0.00002$  ( $2\sigma$ ); for La Jolla Nd it was  $\pm 0.000012$  ( $\pm 0.2 \epsilon_{Nd}$  units); for NBS 981 Pb it was  $\pm 0.011$  for  $^{206}Pb/^{204}Pb$  and  $^{207}Pb/^{204}Pb$ , and  $\pm 0.031$  for  $^{208}Pb/^{204}Pb$ . Within-run  $2\sigma$  errors on the tabulated data were between  $\pm 0.000014$  and  $0.000018$  for  $^{87}Sr/^{86}Sr$ ,  $\pm 0.000005$  and  $0.000010$  for  $^{143}Nd/^{144}Nd$ ,  $\pm 0.004$  and  $0.010$  for  $^{206}Pb/^{204}Pb$  and  $^{207}Pb/^{204}Pb$ , and  $\pm 0.014$  and  $0.028$  for  $^{208}Pb/^{204}Pb$ , and thus less than the external uncertainties on these standards. Total procedural blanks were negligible at  $<36$  pg for Pb,  $<74$  pg for Sr, and  $<18$  pg for Nd. Relative uncertainties ( $2\sigma$ ) for Rb, Sr, Nd, Sm, Pb, U, and Th concentrations measured by isotope dilution are 1%, 0.5%, 0.2%, 0.2%, 0.5%, 1%, and 2%, respectively. Measurements were made at the University of Hawaii and Open University [see Storey *et al.* (1997)]. It should be noted that  $\epsilon_{Nd}=0$  corresponds to  $^{143}Nd/^{144}Nd=0.51264$  today and 0.512531 at 84.4 Ma.

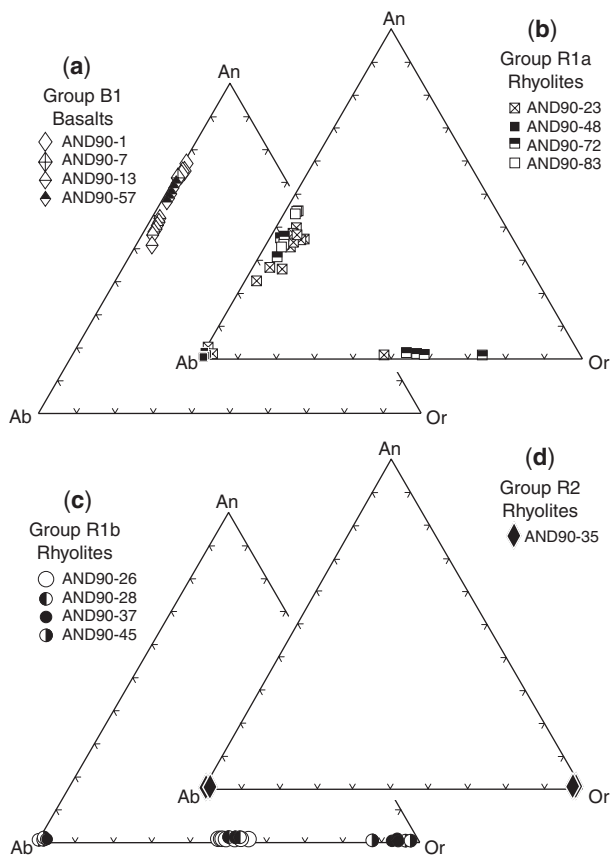


**Fig. 3.** Feldspar ternary diagrams for samples analyzed by electron microprobe: (a) group B1, (b) group R1a; (c) group R1b; (d) group R2. Data are given in Electronic Appendix 2.

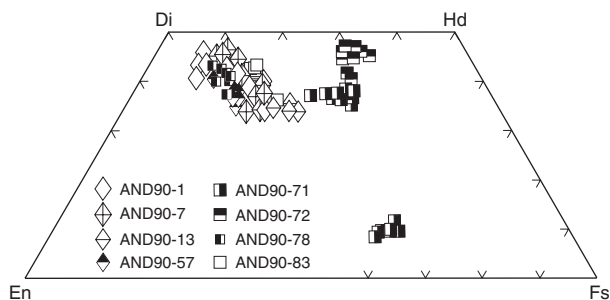


**Fig. 4.** Pyroxene ternary diagram for samples analyzed by electron microprobe. Data are given in Electronic Appendix 2.

### Group R2

The R2 rhyolites are either aphyric or very sparsely aphyric. Where present, phenocrysts are usually subhedral, turbid alkali feldspar with incipient or actual perthite (Fig. 3d), but their abundance is <1% of the total rock. The groundmass comprises microcrystalline to finely crystalline feldspar, quartz, and magnetite. Samples AND90-35, -36, -43, and -53 contain small (<0.2 mm long) laths and blades of blue-green, pleochroic alkali

amphibole, probably arfvedsonite, an amphibole formed under peralkaline conditions. Four samples (AND90-35, -36, -40, -41) contain opaque-rich segregations, and one of these (AND90-40) features a large (3 mm across), skeletal magnetite clot, possibly a pseudomorph after amphibole. Several samples contain trace amounts of minute crystals of zircon.

The groundmass feldspars are pervasively altered, with a dusty, iron-stained appearance, and in some samples the opaque phases (originally magnetite?) are partially replaced by red oxides or oxyhydroxides. Only limited evidence is present for flow alignment of the groundmass phases; most crystal growth appears to have occurred in a stress-free environment. No eutaxitic textures are seen.

### Summary

The two groups of basalt cannot categorically be delineated on the basis of their mineralogy, but olivine was not found in group B2, consistent with the more evolved character of this group (see below). The high-Fo olivine in AND90-1 and -7 is consistent with the relatively high MgO content of these B1 picrites (see below), suggesting that they are not very fractionated. The high NiO content of some of the olivine could suggest derivation from a pyroxene-rich mantle source (see Sobolev *et al.*, 2005).

The R1 rhyolites (and microgranites) are mostly porphyritic, with the dominant phenocrysts being feldspars and quartz. In contrast, the R2 rhyolites are mostly aphyric, and the only phenocryst is alkali feldspar, typically perthitic. In the R1a rhyolites, plagioclase is dominant over alkali feldspar, whereas plagioclase is not found in the R1b rhyolites, consistent with their more evolved, high-silica compositions (see below). Perthitic unmixing is common in feldspars of groups R1b and R2. The majority of the phenocrysts displaying such unmixing are invariably large (>1 mm) and equant, and often show resorption. We infer that they are probably xenocrystic. The R1a rhyolites host a range of pyroxenes, including augite, hedenbergite and pigeonite. Neither R1b nor R2 rhyolites contain pyroxene, but several R2 rhyolites contain small crystals of arfvedsonite. Many rhyolite samples contain accessory zircon, and apatite was identified in the R1a rhyolites.

### Chemical effects of alteration

Some care must be taken in interpreting the chemical data, for alteration has variably but visibly affected all the samples, as noted above. Alteration is reflected in a very general way in LOI values, which range widely from -0.45 to 8.75 wt % for the basaltic samples and from 0.18 to 3.31 wt % for the silicic ones.

As is common in subaerial weathering environments (e.g. Beane *et al.*, 1986; Price *et al.*, 1991), alteration appears to have variably affected K, Na, Rb, and Ba contents in the basaltic samples. Correlations between Ca and more alteration-resistant elements such as Ti or Fe are poor



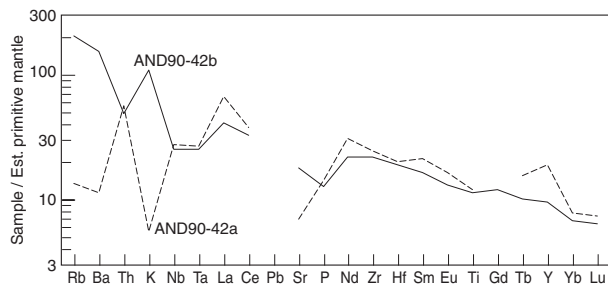


**Fig. 6.** Incompatible-element patterns of two altered samples from a single group B1 flow. Concentrations are normalized to estimated (Est.) primitive mantle values of Sun & McDonough (1989).

Rb, Ba, K, Sr, Y, Na, and Cr, and to a lesser extent in several other trace elements, including some of the rare earth elements (REE).

Some of the variability in Ca, K, and Na contents in the rhyolites (Figs 5c, d and 7e) can be ascribed to post-eruptive mobility, and mobility of SiO<sub>2</sub> is indicated by SiO<sub>2</sub> values greater than 78 wt % in several quartz-poor rhyolites (78 wt % is the maximum observed for unaltered quartz-free rhyolite; e.g. Barker, 1981). In addition, the REE patterns of AND90-32 and -61 display sizeable negative Ce anomalies (Fig. 8h). These anomalies may reflect alteration in which Ce was mobilized in its +4 oxidation state, although the alteration in these samples appears superficially rather similar to that in some samples without Ce anomalies; alternatively, the anomalies may result from removal of trace amounts of unusual REE-rich accessory minerals (which, however, we did not see in the thin sections) during late-stage magmatic evolution. Miller & Harris (2007) also noted Ce anomalies in several of their samples from the Lebombo area of the Karoo province.

## Geochemistry of the basaltic rocks

### Group B1

This group includes both basalt and basaltic andesite. Most of the B1 rocks have low MgO (1.83–5.59 wt %), Mg-number (23–53, =  $[100 \times \text{molar Mg}/(\text{Mg} + \text{Fe}^{2+})]$ , assuming Fe<sub>2</sub>O<sub>3</sub> is 13% of total iron oxide), and Ni (6–101 ppm). However, dike sample AND90-1 and flow sample AND90-7 have much higher values (12.14 and 13.19 wt % MgO, Mg-numbers of 70 and 71, and 305 and 382 ppm Ni, respectively), consistent with their high-Fo olivine phenocrysts. Silica content ranges from 48.5 to 58.0 wt %, but three of the four samples with SiO<sub>2</sub> > 54.6 wt % have very high LOI (4.13–7.50 wt %) and we suspect that alteration may have modified their SiO<sub>2</sub> values. Data for all but four B1 samples fall below the line dividing tholeiitic and alkalic Hawaiian lavas in Fig. 5a; the high total alkali contents in the other four samples are likely to reflect local alteration-related enrichment (e.g. AND90-42b; Fig. 6).

All of the B1 rocks are moderately enriched in the light REE (LREE) relative to the middle (MREE) and heavy REE (HREE) (Fig. 8f). For example, chondrite-normalized  $(\text{La}/\text{Sm})_{\text{ch}} = 1.7\text{--}3.2$  and  $(\text{La}/\text{Yb})_{\text{ch}} = 3.5\text{--}8.6$ ; the lowest values (and flattest REE patterns) are exhibited by the two high-MgO samples. Europium anomalies range from absent to slightly negative. Primitive-mantle-normalized incompatible element patterns exhibit a Nb–Ta trough, with normalized  $(\text{Nb}/\text{La})_{\text{pm}}$  between 0.40 and 0.70 (Fig. 8a). Other notable features are sizeable peaks at Pb and troughs at P. With rare exceptions (e.g. high-MgO sample AND90-1), Sr is variably depleted relative to Nd. Broadly similar patterns are seen elsewhere in southern Madagascar in lava flows in the Morondava Basin and tholeiitic dikes of the Ejeda–Bekily swarm (Mahoney *et al.*, 1991; Dostal *et al.*, 1992).

Age-corrected isotope ratios define an array that partly overlaps, but is distinct from, that of the tholeiitic lavas of southwestern Madagascar. The B1 samples cover a wide range of  $\epsilon_{\text{Nd}}(t)$  and  $(^{87}\text{Sr}/^{86}\text{Sr})_t$ , from –2.5 to –13.2 and 0.70915 to 0.71500, respectively (Fig. 9a), and the values correlate roughly with degree of LREE enrichment [e.g. increasing  $(^{87}\text{Sr}/^{86}\text{Sr})_t$  and decreasing  $\epsilon_{\text{Nd}}(t)$  are accompanied by decreasing  $^{147}\text{Sm}/^{144}\text{Nd}$  and increasing  $(\text{La}/\text{Sm})_{\text{ch}}$ ]. Both the highest and lowest  $\epsilon_{\text{Nd}}(t)$  values are from dikes, whereas four of the five B1 lavas analyzed from the Vohitsimbe section display only a narrow range of  $\epsilon_{\text{Nd}}(t)$ , from –6.5 to –7.0. Relative to ocean ridges and islands, all of the B1 rocks have high  $(^{207}\text{Pb}/^{204}\text{Pb})_t$  (15.82–15.96) and  $(^{208}\text{Pb}/^{204}\text{Pb})_t$  (39.39–40.94) for their  $(^{206}\text{Pb}/^{204}\text{Pb})_t$  values (18.09–18.92). Their Pb isotope ratios do not correlate well with each other (Fig. 9d–f) or with either Nd (Fig. 9b) or Sr isotope ratios. This cannot be ascribed simply to over- or under-correction in the age adjustment for Pb as a result of alteration-related modification of U/Pb and/or Th/Pb. For example, values of  $^{207}\text{Pb}/^{204}\text{Pb}$  have changed little since 84 Ma from radiogenic ingrowth ( $^{235}\text{U}$ , the parent isotope of  $^{207}\text{Pb}$ , is only 0.7 atom% of  $^{238}\text{U}$ ) and are thus insensitive to post-eruptive alteration of the U/Pb ratio; yet the full range of  $(^{207}\text{Pb}/^{204}\text{Pb})_t$  from 15.82–15.96 is observed among samples with closely similar  $\epsilon_{\text{Nd}}(t)$  values, between –6.5 and –7.2 (Fig. 9c).

### Group B2

Like most of the B1 samples, the B2 rocks are evolved, with MgO between 3.55 and 6.60 wt %, Mg-number between 36 and 54, and 27–95 ppm Ni. However, they are lower in SiO<sub>2</sub> (46.92–50.65 wt %) and mildly alkalic (Fig. 5a). They also are more LREE-enriched (Fig. 8g), with  $(\text{La}/\text{Sm})_{\text{ch}} = 3.0\text{--}3.7$  and  $(\text{La}/\text{Yb})_{\text{ch}} = 11\text{--}14$ . Europium anomalies are absent. Values of  $(\text{Nb}/\text{La})_{\text{pm}}$  are higher (0.85–0.92) than in group B1, and the incompatible-element patterns lack Nb–Ta troughs (Fig. 8b). Strontium troughs are also lacking, and peaks at Pb vary from absent

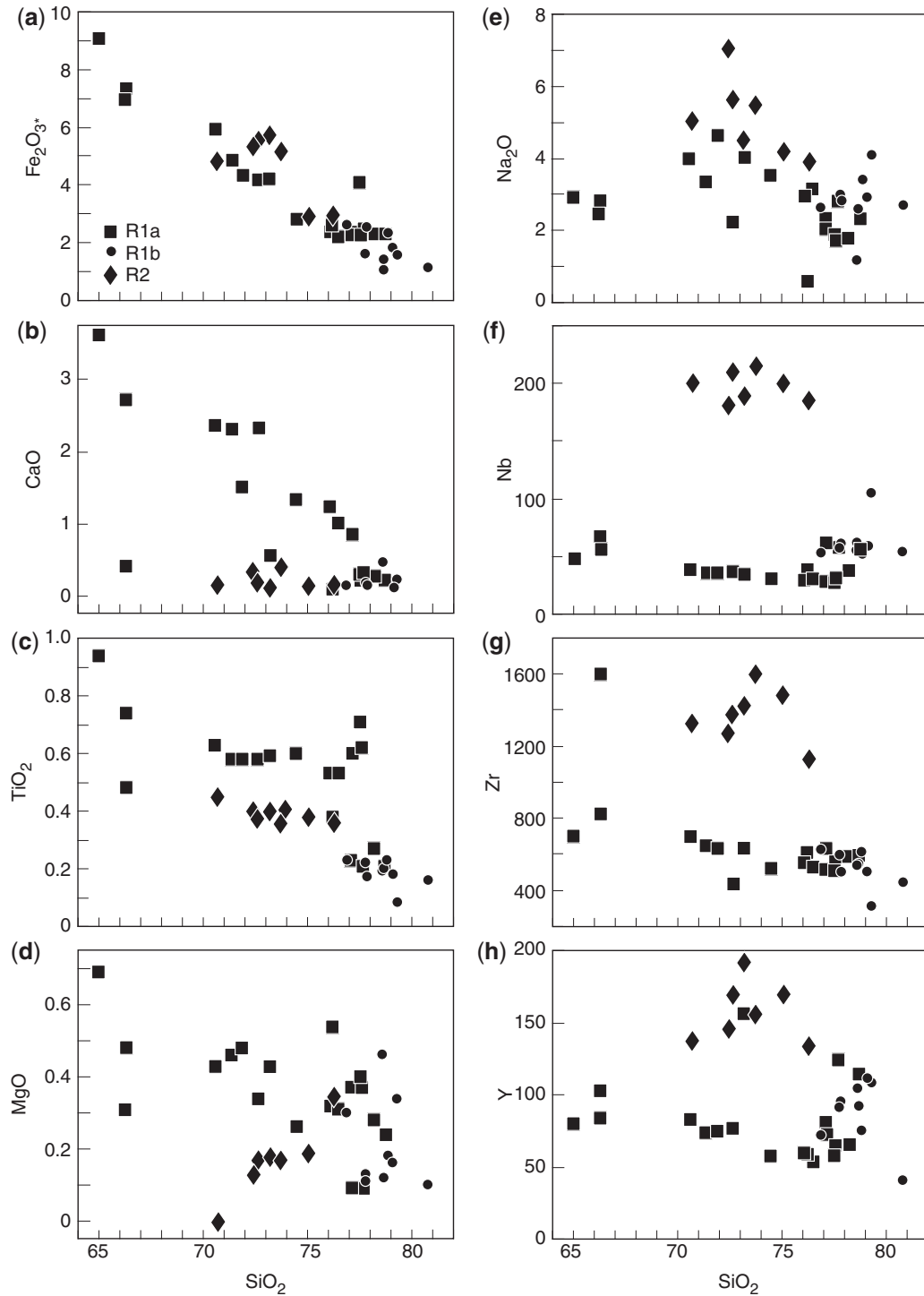


**Fig. 7.** Selected element variations vs  $\text{SiO}_2$  among the silicic samples. Major element values are in wt %, trace elements in ppm.

to modest; however, as with the B1 rocks, a sizeable trough at P is consistently present. Broadly similar patterns are displayed by some alkalic basalt dikes in the Ejeda–Bekily swarm. However, the dikes tend to have large peaks at Ba (Dostal *et al.*, 1992) that are not present in the B2 patterns.

The B2 basalts are also isotopically distinct from the Ejeda–Bekily dikes (Fig. 9). They differ from the B1 samples in having higher  $\epsilon_{\text{Nd}}(t)$  (+0.6 to –2.4) and lower  $(^{87}\text{Sr}/^{86}\text{Sr})_t$  (0.70579–0.70734). Ratios of  $(^{206}\text{Pb}/^{204}\text{Pb})_t$  (18.20–18.63) are within the B1 range but  $(^{207}\text{Pb}/^{204}\text{Pb})_t$

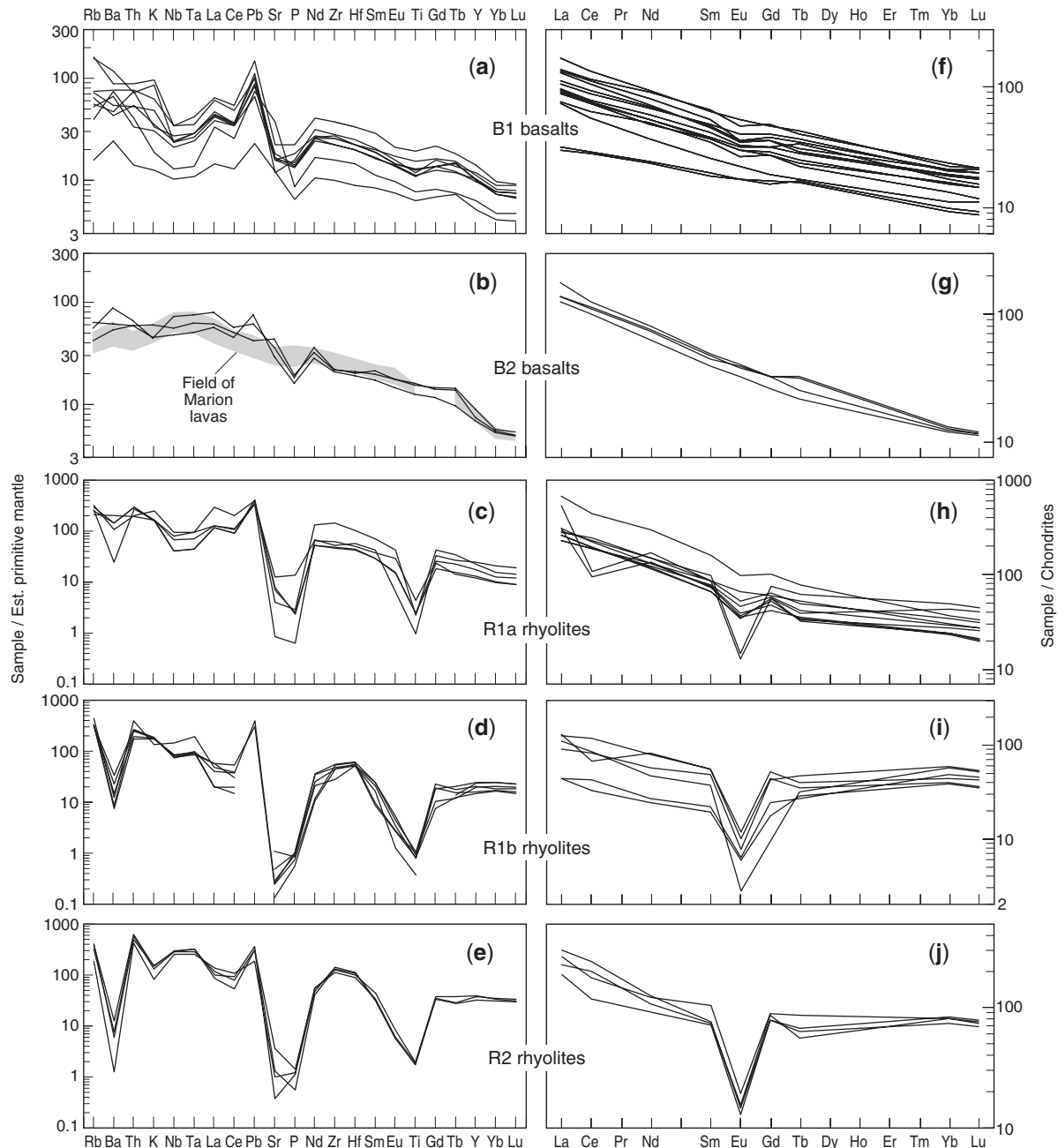


**Fig. 8.** Incompatible-element patterns of selected group B1 (a), B2 (b), R1a (c), R1b (d), and R2 (e) samples, including samples that were analyzed for isotope ratios. Shading in (b) represents the range of values for recent lavas of the Marion hotspot (Storey *et al.*, 1997; Janney *et al.*, 2005). (f–j) show corresponding chondrite-normalized REE patterns. Data are given in Tables 1 and 2, and Electronic Appendices 3 and 4.

(15.66–15.70) is much lower;  $(^{208}\text{Pb}/^{204}\text{Pb})_t$  also extends to lower values (to 39.29).

### Geochemistry of the silicic rocks

Most of the silicic samples are subaluminous; a few are mildly peralkaline. Like the basalts, they define two compositionally distinct groups (see Storey *et al.*, 1997). Group R1 has much lower Th, Nb, Ta, Zr, Hf, Y, and HREE

concentrations than R2 (e.g. Nb = 27–105 ppm in R1 vs 182–215 ppm in R2). The R1 samples also tend to have lower  $\text{Na}_2\text{O}$  and higher  $\text{TiO}_2$ ,  $\text{P}_2\text{O}_5$ , and CaO for a given  $\text{SiO}_2$  content than the R2 samples (Fig. 7).

#### Group R1

Two compositional sub-types are present within R1: R1a and R1b. A diagnostic feature of R1a is a trough at Nb

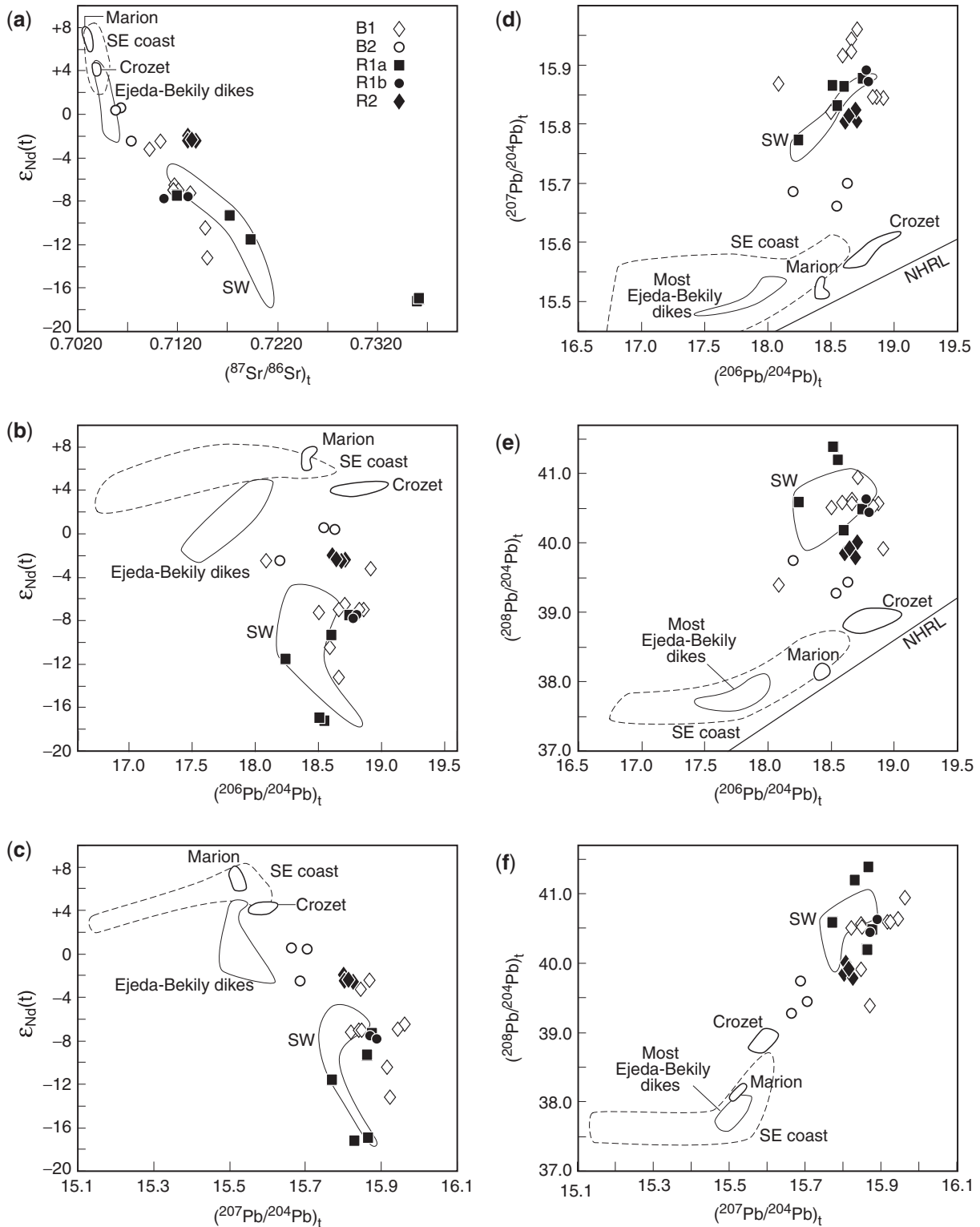


**Fig. 9.** Age-corrected Nd, Pb, and Sr isotope data for Androy samples. Fields for tholeiitic basalt flows and dikes of SW Madagascar, alkalic dikes of the Ejeda-Bekily swarm, most SE coastal basalts, and modern Marion and Crozet hotspots are from data of Mahoney *et al.* (1991, 1992, 1996) and Storey *et al.* (1997). NHRL in (d) and (e) is the Northern Hemisphere reference line (Hart, 1984), defined by several groups of oceanic islands and most ocean ridge basalts north of the Equator. Data are given in Table 3 and Electronic Appendix 5.

and Ta in Fig. 8c, with  $(\text{Nb/La})_{\text{pm}} = 0.16\text{--}0.68$ . In this important respect, the R1a incompatible-element patterns are similar to those of the B1 basalts. Large troughs at Ti, P, and Sr are present, as are a variably negative Eu anomaly and a prominent peak at Pb. Several R1a samples also have pronounced troughs at Ba. In addition to rhyolite with  $\text{SiO}_2 > 70$  wt %, R1a includes three samples of trachydacite with 65.00–66.29 wt %  $\text{SiO}_2$  (Fig. 5a). Trachydacite AND90-23 has an incompatible-element pattern closely resembling those of several of the rhyolites. The pattern of AND90-18 is similar, but exhibits the largest Nb–Ta trough of group R1a; this sample also has the highest  $(\text{La/Yb})_{\text{ch}}$  ratio and highest Zr, Hf, and MREE and LREE concentrations of the group.

The R1b samples are all rhyolites, and were found only in the Vohitsimbe section, interbedded with R1a and B1 units. They reach higher  $\text{SiO}_2$  and lower  $\text{TiO}_2$  and total iron than group R1a (Figs 5 and 7), are characterized by distinctly higher  $(\text{Nb/La})_{\text{pm}}$  (1.3–4.2; Fig. 8d), and their incompatible element patterns display variable-size peaks at Zr and Hf relative to Nd and Sm, which are lacking in R1a patterns. Troughs at Ba are generally larger than seen among the R1a samples. So too, in many cases, are those at Ti, P, Sr, and Eu (all relative to Zr–Hf). Also, the R1b rhyolites are much less enriched in the LREE relative to the HREE [ $(\text{La/Yb})_{\text{ch}} = 0.97\text{--}3.4$  for R1b vs 6.0–19 for R1a; see Fig. 8h and i], whereas concentrations of Yb, Lu, and Y tend to be somewhat higher than in most R1a samples at similar  $\text{SiO}_2$  (e.g. Fig. 7h).

The R1a isotope data form a trend that, with decreasing  $\epsilon_{\text{Nd}}(t)$ , departs from the B1 array toward higher  $(^{87}\text{Sr}/^{86}\text{Sr})_i$  and reaches the lowest  $\epsilon_{\text{Nd}}(t)$  and by far the highest  $(^{87}\text{Sr}/^{86}\text{Sr})_i$  values of any of the Androy rocks (Fig. 9a). The most extreme values are exhibited by a dike on the southeastern side of the massif (AND90-6) and a flow within the upper part of the Rim Series on the northeastern side (AND90-83); this flow is stratigraphically the lowest of the rhyolite flows we sampled. These two rhyolites have closely similar  $\epsilon_{\text{Nd}}(t) = -17.0$  and  $-17.3$  and  $(^{87}\text{Sr}/^{86}\text{Sr})_i = 0.73602$  and  $0.73622$ . They also have very similar age-corrected Pb isotope ratios, virtually identical incompatible-element patterns, and very similar major element compositions. The AND90-6 dike thus may be a feeder of the AND90-83 flow. Their  $(^{206}\text{Pb}/^{204}\text{Pb})_i$  and  $(^{207}\text{Pb}/^{204}\text{Pb})_i$  values are within the B1 basalt range, but their  $(^{208}\text{Pb}/^{204}\text{Pb})_i$  values (41.19, 41.39) are higher (Fig. 9b–e). The other three R1a samples we analyzed isotopically, including trachydacites AND90-18 and -23, have lower  $(^{208}\text{Pb}/^{204}\text{Pb})_i$  (40.18–40.58) and  $(^{87}\text{Sr}/^{86}\text{Sr})_i$  (0.7121–0.7194), and less negative  $\epsilon_{\text{Nd}}(t)$  ( $-7.5$  to  $-11.6$ ). In this respect, they are more similar to the B1 basalts.

We measured isotope ratios for two R1b rhyolites (AND90-27, AND90-29), both from the upper levels at Vohitsimbe (Fig. 10). Values for both samples are very

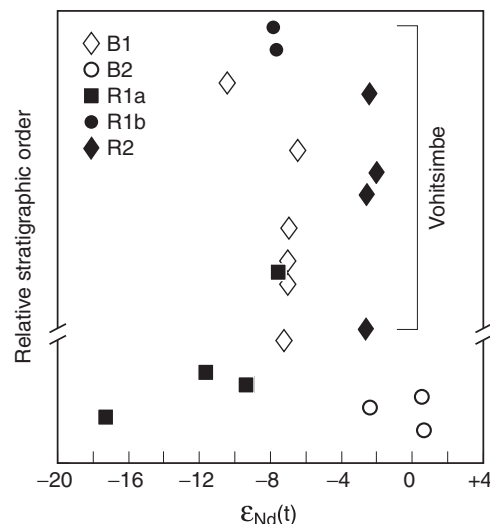


**Fig. 10.** Variation of  $\epsilon_{\text{Nd}}(t)$  with relative stratigraphic order. (Note the break in the  $y$ -axis below the Vohitsimbe section, indicating that stratigraphic control is rather poor below this section.)

similar to those for the highest- $\epsilon_{\text{Nd}}(t)$  R1a rhyolite (AND90-48, also from Vohitsimbe) in all panels of Fig. 9. Moreover, values for these three rhyolites are similar to those of four of the five Vohitsimbe B1 basalts we analyzed isotopically [e.g.  $\epsilon_{\text{Nd}}(t) = -7.5$  to  $-7.8$  for the rhyolites and  $-6.5$  to  $-7.0$  for the basalts]. The one B1 lava from a stratigraphic level below the Vohitsimbe section that we analyzed isotopically also has similar  $\epsilon_{\text{Nd}}(t)$  ( $-7.2$ ) (Fig. 10).

### Group R2

Although the R2 rhyolites have much higher concentrations of HREE, Th, Nb, Ta, Zr, Hf, and Y than group R1, their incompatible element patterns are similar in overall shape to those of the R1b samples, with peaks at Nb–Ta and Zr–Hf, and large troughs at Ba, Sr, P, Eu, and Ti (Fig. 8e). As with group R1b, the relative enrichment in the LREE (e.g.  $(\text{La/Yb})_{\text{ch}} = 2.4\text{--}4.4$ ) is significantly less than for the R1a samples (Fig. 8j).

The four R2 flows we analyzed isotopically are all from the Vohitsimbe section, and have closely similar age-corrected isotope ratios. These samples define a Rb–Sr isochron with initial  $(^{87}\text{Sr}/^{86}\text{Sr})_i = 0.71348 \pm 0.00054$  and an age of  $84.0 \pm 2.4$  Ma ( $2\sigma$ ); the mean square of weighted deviates (MSWD) is 2.3 (Fig. 11). No correlation of age-corrected  $(^{87}\text{Sr}/^{86}\text{Sr})_i$  with  $1/\text{Sr}$  or  $^{87}\text{Rb}/^{86}\text{Sr}$  is present, suggesting that the isochron is not a mixing line. Indeed, the Rb–Sr age is identical, within error, to Storey *et al.*'s (1995)  $^{40}\text{Ar}\text{--}^{39}\text{Ar}$  age of  $84.4 \pm 1.0$  Ma ( $2\sigma$ ) for sanidine from Vohitsimbe R1b rhyolite AND90-27. (Interestingly, a Rb–Sr age of  $84.6 \pm 1.5$  Ma is obtained from R1b samples AND90-27 and -29, R1a sample AND90-48, and B1 samples AND90-23 and -49B, all of which are from the Vohitsimbe section and have, in addition to Sr, similar

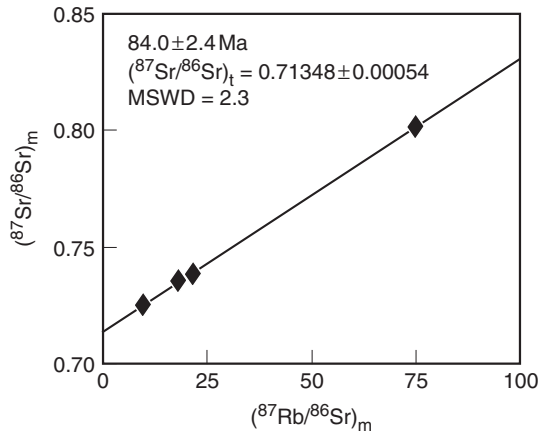


**Fig. 11.** Rb–Sr isochron diagram for R2 rhyolites. The isochron was calculated using the equations of York (1969) and assuming errors in  $x$  and  $y$  values are uncorrelated. MSWD, mean square of weighted deviates.

age-corrected Nd and Pb isotope ratios; however, the MSWD is large, at 11.5.)

Age-corrected  $\epsilon_{\text{Nd}}(t)$  values of three of the R2 samples, AND90-34, -43, and -53, are identical within error ( $-2.4$  to  $-2.6$ ) and that for AND90-41 ( $-2.0$ ) is only slightly higher. However, unlike their measured  $^{87}\text{Sr}/^{86}\text{Sr}$  and  $^{87}\text{Rb}/^{86}\text{Sr}$  values, variation in measured  $^{143}\text{Nd}/^{144}\text{Nd}$  and  $^{147}\text{Sm}/^{144}\text{Nd}$  is small, so that no Sm–Nd isochron is developed. In Fig. 9a, the age-corrected Nd–Sr isotope data for the R2 rhyolites cluster to the right of the array formed by the B1 and B2 basalts. Age-corrected Pb isotope ratios cover a slightly larger total range than the present-day values (e.g. 0.10 vs 0.05 for  $^{208}\text{Pb}/^{204}\text{Pb}$ ), suggesting some relatively recent disturbance of U/Pb and Th/Pb ratios in some of the R2 samples, probably as a result of weathering-related alteration (e.g. Rosholt *et al.*, 1971; Doe *et al.*, 1982). Nevertheless, the total variation in age-corrected  $(^{206}\text{Pb}/^{204}\text{Pb})_b$ ,  $(^{207}\text{Pb}/^{204}\text{Pb})_b$  and  $(^{208}\text{Pb}/^{204}\text{Pb})_i$  is small: 18.61–18.71, 15.80–15.82, and 39.78–40.00, respectively (Fig. 9b–e).

## DISCUSSION

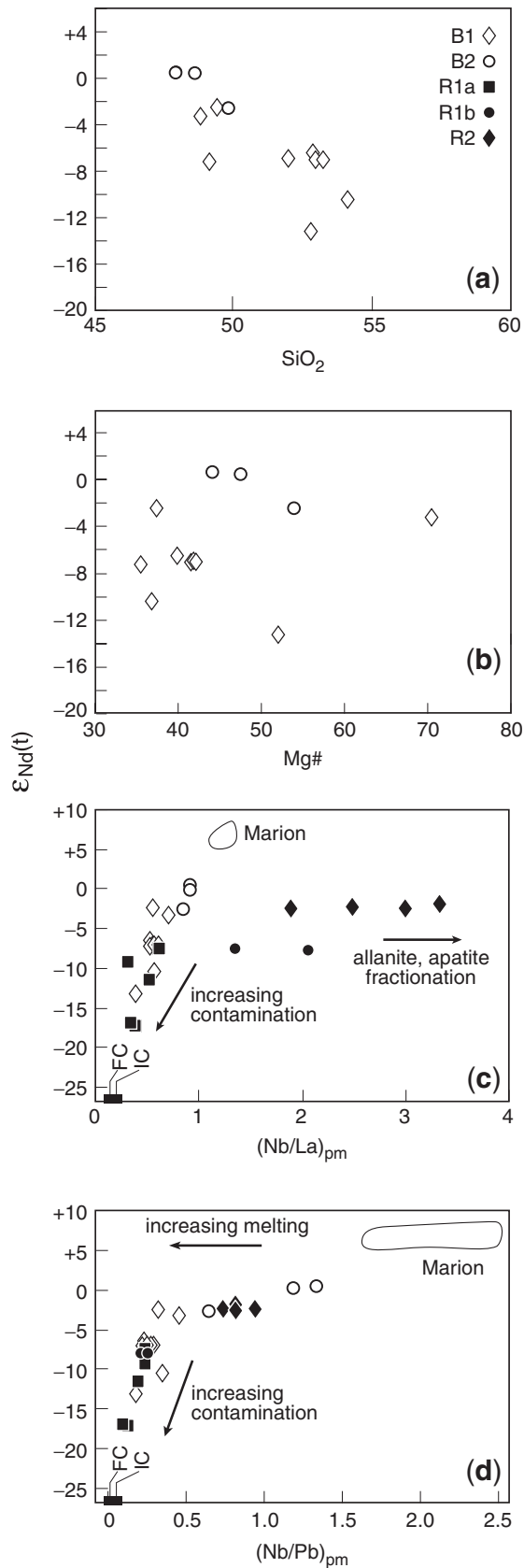
### Origin of the basaltic rocks

A substantial role for continental components in the genesis of group B1 is indicated by the combination of variable but low  $\epsilon_{\text{Nd}}(t)$ , high  $(^{87}\text{Sr}/^{86}\text{Sr})_b$ ,  $(^{207}\text{Pb}/^{204}\text{Pb})_b$  and  $(^{208}\text{Pb}/^{204}\text{Pb})_b$  and incompatible element patterns with Nb–Ta troughs and Pb peaks. The same is true for tholeiitic basalts in southwestern Madagascar (Mahoney *et al.*, 1991; Dostal *et al.*, 1992). Assuming the B1 magmas originated from a relatively homogeneous mantle source with higher  $\epsilon_{\text{Nd}}$  than measured for any of our samples, the Pb isotope data imply considerable heterogeneity in  $^{206}\text{Pb}/^{204}\text{Pb}$  in the low- $\epsilon_{\text{Nd}}$  continental material that

affected the magmas (Fig. 9b). In contrast, the coherent array in Fig. 9a indicates relative Nd and Sr isotope homogeneity for this material. The isotopic and chemical characteristics of basement crust and lithospheric mantle in this region of Madagascar are essentially unknown. However, a rough positive correlation is present between  $(^{87}\text{Sr}/^{86}\text{Sr})_t$  and  $\text{SiO}_2$ , and a negative one between  $\epsilon_{\text{Nd}}(t)$  and  $\text{SiO}_2$  (Fig. 12a), suggesting that the low- $\epsilon_{\text{Nd}}$  material was crust rather than lithospheric mantle. Some indirect support that it was not mantle peridotite may be provided by the R1 rhyolites, which are interbedded with the B1 basalts, appear to be related petrogenetically to them (see below), and reach even lower  $\epsilon_{\text{Nd}}(t)$ ; rhyolites do not form by melting of peridotite (e.g. Yöder, 1973). Because B1 (and B2) dikes are present in and around the Androy massif, the basalt flows were probably erupted from relatively nearby feeders. Given that basement exposed in the vicinity is largely Archean, the continental material affecting the B1 basalts is also likely to have been Archean.

Isotope ratios among the B1 basalts do not correlate with Mg-number (Fig. 12b), implying that no particular impediment existed to post-contamination differentiation of B1 magmas and/or that contamination could occur at different stages of differentiation (for example, contamination might occur at a deeper crustal level, followed by magma movement to a shallower level where further fractional crystallization could occur). The apparent abundance of B1 basalts with  $\epsilon_{\text{Nd}}(t)$  near  $-7$  in the thick Vohitsimbe section (Fig. 10) may reflect an open magmatic system in which recharge, fractionation, and contamination reached a near-steady state (e.g. O'Hara & Mathews, 1981; Wooden *et al.*, 1993; Peng *et al.*, 1994) during the later stages of Androy volcanism. That the lowest- $\epsilon_{\text{Nd}}$  Androy rocks are rhyolites and that rhyolites underlie and are interbedded with the B1 basalts even raises the question of whether contamination of B1 magmas could have occurred through admixture with low- $\epsilon_{\text{Nd}}$  R1-type silicic liquids rather than by bulk or selective assimilation of crustal wall rock. Indeed, the B1 and R1a data define a negative correlation of  $\epsilon_{\text{Nd}}(t)$  with ratios such as  $(\text{Nb}/\text{La})_{\text{pm}}$  and  $(\text{Nb}/\text{Pb})_{\text{pm}}$  (Fig. 12c and d), qualitatively consistent with such mixing. However, leaving aside questions of the physical feasibility of such a process on the large scale appropriate for Androy (e.g. Snyder, 2000), we can reject mixing between B1 magmas and the lowest- $\epsilon_{\text{Nd}}$  R1-type liquids as the main contamination mechanism. For example, although the R1 rhyolites reach higher  $(^{208}\text{Pb}/^{204}\text{Pb})_i$  and  $(^{87}\text{Sr}/^{86}\text{Sr})_i$  than the basalts, the basalts attain higher  $(^{207}\text{Pb}/^{204}\text{Pb})_i$  than any of the rhyolites (Fig. 9).

The characteristics of group B2—higher  $\epsilon_{\text{Nd}}(t)$  and lower  $(^{87}\text{Sr}/^{86}\text{Sr})_b$ ,  $(^{207}\text{Pb}/^{204}\text{Pb})_b$ ,  $(^{208}\text{Pb}/^{204}\text{Pb})_b$  and  $\text{SiO}_2$  than B1, incompatible element patterns that lack Nb–Ta troughs and lack significant Pb peaks—suggest that the B2 basalts are less contaminated than the B1 rocks.



The stratigraphic location of the B2 flows below the B1 flows suggests the possibility that B2 magma could have been the high- $\epsilon_{\text{Nd}}(t)$  mixing end-member for group B1. Such a relationship is permitted by our isotopic results but not supported by the chemical data. For example, although the B2 and B1 data lie along a single trend in Fig. 12c, they diverge at a high angle in Fig. 12d. Likewise, B1 sample AND90-1 and B2 sample AND90-78 have similar Nd isotope ratios (within 0.9  $\epsilon_{\text{Nd}}$  units of each other), but the B1 rock has much lower concentrations of incompatible elements (Table 2) and an incompatible-element pattern with a flatter overall slope from Lu to Rb. With the exception of Nb and Ta, contamination by typical Archean mafic to felsic crust (e.g. Rudnick & Fountain, 1995) would increase, not decrease, the magmatic concentrations of the highly incompatible elements and would not flatten the slope of the pattern from Lu to Rb. However, it remains possible that the B2 magmas were generated by smaller amounts of partial melting in the same mantle source as the B1 basalts. The overall slopes (although not all the details) of the incompatible element patterns of the B2 basalts and least contaminated, high- $\epsilon_{\text{Nd}}(t)$  B1 basalts are matched reasonably well by model patterns that assume a single source and different amounts of partial melting in the garnet and spinel facies (e.g. Fig. 13).

Were any of the Androy basalts derived from Marion hotspot mantle? As noted above, plate reconstructions suggest that the hotspot was near this part of Madagascar at 84 Ma (Fig. 1b). The two picritic high-MgO B1 samples (AND90-1 and -7) with forsteritic olivine (up to Fo<sub>91.8</sub>) are consistent with a (thermal) plume source, and the high NiO content of their olivine phenocrysts could suggest a source relatively rich in pyroxenite (see Sobolev *et al.*, 2005). None of the Androy samples have isotopic signatures resembling those of recent products of the Marion hotspot; nor are they similar to those of the Crozet hotspot, ~500 km east of Marion. However, the B2 basalts possess more ocean-island-like isotopic ratios and incompatible element patterns than those of group B1, and in all panels of Fig. 9 the B2 data points, particularly those of the two highest- $\epsilon_{\text{Nd}}(t)$  samples, lie broadly between the B1 (and rhyolite) data and the fields for Marion and Crozet. The same is true in Fig. 12c, which shows  $\epsilon_{\text{Nd}}(t)$  vs  $(\text{Nb}/\text{La})_{\text{pm}}$ ; the Nb/La ratio is relatively insensitive to variation in the amount of mantle melting, as Nb and La have very similar bulk distribution coefficients in most mantle rock types. Thus, it is possible that Androy magmas contained

**Fig. 12.**  $\text{SiO}_2$  (a) and Mg-number (b) vs  $\epsilon_{\text{Nd}}(t)$  for B1 and B2 samples. Variation of  $\epsilon_{\text{Nd}}(t)$  with  $(\text{Nb}/\text{La})_{\text{pm}}$  (c) and  $(\text{Nb}/\text{Pb})_{\text{pm}}$  (d) for all samples. Arrows schematically illustrate the effects of increasing contamination by low- $\epsilon_{\text{Nd}}$  continental crust, removal of allanite and/or apatite, and increasing amounts of partial melting. FC and IC indicate  $(\text{Nb}/\text{La})_{\text{pm}}$  and  $(\text{Nb}/\text{Pb})_{\text{pm}}$  values of global average Archean felsic and intermediate crust, respectively (Rudnick & Fountain, 1995).

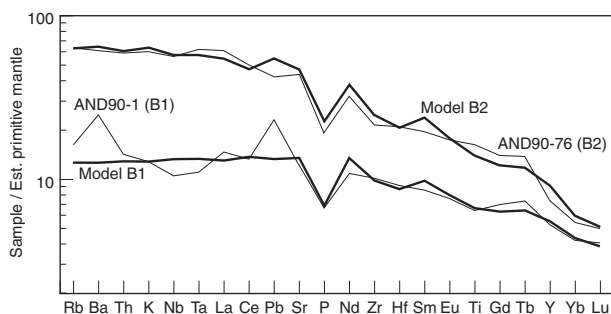


**Fig. 13.** Incompatible-element patterns of high- $\epsilon_{Nd}(t)$  basalts AND90-1 (group B1) and AND90-76 (B2) compared with patterns of model partial melts. The model B1 pattern is for a 50:50 mix of a 4% fractional melt (Shaw, 1970) of garnet peridotite and a 7% melt of spinel peridotite. The Model B2 pattern is for a 70:30 mix of a 4% melt of garnet peridotite and a 1.5% melt of spinel peridotite. Element concentrations in the model garnet peridotite source are those estimated for primitive mantle by Sun & McDonough (1989), except for P, which is assigned a concentration half the estimated primitive mantle value. The starting spinel peridotite is assumed to have trace element concentrations corresponding to the residue of 4% of garnet-facies melting. The model garnet peridotite is 60% olivine, 21% orthopyroxene, 8% clinopyroxene, and 11% garnet, melting in proportions of 0.01, 0.09, 0.36, and 0.54, respectively; the model spinel peridotite is 52% olivine, 27% orthopyroxene, 18% clinopyroxene, and 3% spinel, which melt in proportions of -0.06, 0.28, 0.67, and 0.11, respectively, after Niu *et al.* (1996). Distribution coefficients are taken or interpolated from Salters & Stracke (2004). No adjustment has been made for magmatic differentiation in the B1 model pattern (consistent with the Mg-number of 70 of AND90-1), whereas concentrations in the B2 model pattern have been multiplied by 1.7 to bring the pattern's Lu value to that of AND90-76 (with Mg-number of 44).

a hotspot-derived component, although the isotopic data certainly do not require this.

Significantly, the B2 incompatible-element patterns all exhibit a prominent trough at P (Fig. 8b). Melting in the garnet stability field may produce a P trough (Haggerty *et al.*, 1994); however, modern Marion hotspot lavas, which appear to have formed in the presence of residual garnet (Storey *et al.*, 1997; Janney *et al.*, 2005), lack P troughs. Moderate to large amounts of magmatic contamination by many types of continental crust can produce a trough at P, but also commonly generate a large peak at Pb, a Nb-Ta trough, and sometimes a trough at Sr or Ti (e.g. Cox & Hawkesworth, 1984; Wooden *et al.*, 1993; Peng *et al.*, 1994), none of which are present in the B2 patterns. Weathering-related alteration can redistribute P in basalts (e.g. Fodor *et al.*, 1992) and, as noted above, the basalts with the highest LOI values exhibit greater variability in P content. However, despite the variable alteration in the B2 samples (e.g. LOI ranges from 0.24 to 2.81 wt % among the B2 samples analyzed for trace elements), the size of the P trough is rather constant. Phosphorus troughs can also develop by removal of apatite during differentiation, but P increases with decreasing MgO in both groups B2 and B1 (Fig. 5e), implying little removal of apatite from the basaltic magmas; none was seen in thin section.

We conclude that the P trough is probably largely a mantle source feature. If so, the B2 basalts were derived from a source at least partly distinct from that feeding recent Marion hotspot magmas. The difference could indicate a component in the hotspot source during the middle Cretaceous that is no longer present. Alternatively, as proposed for the alkalic dikes in the Ejeda-Bekily swarm (Mahoney *et al.*, 1991; Dostal *et al.*, 1992), the B2 basalts may represent partial melts of lithospheric mantle, or hotspot-derived magmas that interacted significantly with such mantle. Interestingly, most of the alkalic Ejeda-Bekily dikes have a P trough, although their isotopic differences from the B2 basalts (Fig. 9) indicate a separate petrogenesis. Phosphorus troughs are also a feature of all the B1 patterns (e.g. Fig. 8a), supporting the possibility that groups B1 and B2 are related by different amounts of partial melting of a common source.

### Origin of the rhyolites

Rhyolites in predominantly basaltic continental volcanic provinces are attributed to some combination of extreme crystal fractionation (with or without assimilation of wall rock) and crustal melting (with or without mixing of melts with more mafic mantle-derived magmas). In the category of crustal melting, both melting of old crustal rock and of solidified basalt intruded within or underplated to the crust during the same volcanic episode can occur (e.g. Sethna & Battiwala, 1974; Doe *et al.*, 1982; Cleverly *et al.*, 1984; Bellieni *et al.*, 1986; Lightfoot *et al.*, 1987; Harris *et al.*, 1990; Leeman *et al.*, 1992; Garland *et al.*, 1995; Cameron *et al.*, 1996; Harris & Milner, 1997; Kirstein *et al.*, 2000; Riley *et al.*, 2001; Miller & Harris, 2007). Modeling indicates that large amounts of rhyolite can be generated when basalt repeatedly invades a region of crust over a period of  $10^5$ – $10^6$  years, and suggests that partial melting of basalt and/or older crustal wall rock will typically occur together with the simultaneous generation of highly fractionated liquids by crystallization of basaltic magma (Annen & Sparks, 2002; Annen *et al.*, 2006). Evidence from O isotopes, U-series isotopes, and combined major and trace element compositions in Iceland, where old continental crust is not a factor, indicates that either fractionation or melting can be the dominant process, depending on the volcanic system (e.g. Sigmarsson *et al.*, 1991; Furman *et al.*, 1992; Jónasson, 1994; Selbekk & Trønnes, 2007).

### Group R1

As with the basalts, we infer from the presence of R1 dikes that the R1 flows were erupted from relatively nearby vents. The overlap of the Vohitsimbe R1a and R1b isotope ratios with B1 values, the Nb-Ta troughs in the R1a and B1 incompatible-element patterns, and the interbedding of B1 and R1 flows strongly suggest that group R1 is related petrogenetically to group B1. A petrogenetic association is also suggested by element ratios such as Nb/Pb

(e.g. Fig. 12d), which should not be affected much by fractionation of most of the minerals observed in these rhyolites (i.e. plagioclase, Fe–Ti oxides, clinopyroxene, apatite, and quartz). Within the Vohitsimbe section, four of the five B1 samples and all three R1 samples that we analyzed isotopically possess similar age-corrected Nd, Sr, and Pb isotope ratios; for example, the full range of  $\epsilon_{\text{Nd}}(t)$  measured is only 1.3 units (from  $-6.5$  to  $-7.8$ ) (Fig. 10). These R1 rhyolites are therefore likely to have been derived by advanced crystallization of B1 magma or remelting of earlier-intruded B1 basalt followed by fractional crystallization, with relatively little additional assimilation of old crustal wall rock.

Neither process is constrained very strongly by our data. No isotopically equivalent rocks were found among the few samples of intermediate composition, and major element modeling, in particular, is hampered by the alteration effects discussed above. However, simple major-element mass balance following Stormer & Nicholls (1978) suggests that 75–95% crystal fractionation of an assemblage consisting of plagioclase, clinopyroxene, magnetite and/or ilmenite, alkali feldspar, and apatite would be needed to produce the Vohitsimbe R1 rhyolites from the B1 basalts (the lowest residuals are achieved by assuming an intermediate stage corresponding to one of the rare trachydacites, but it should be remembered that the  $\epsilon_{\text{Nd}}(t)$  values of the trachydacites ( $-9.4$ ,  $-11.6$ ) indicate a significantly greater crustal component than in the Vohitsimbe R1 rhyolites). The scarcity of intermediate compositions (Fig. 5a), termed the ‘silica gap’, is a feature common to many basalt–rhyolite associations, and often taken as evidence for rhyolite formation by melting of basaltic precursors. However, it also may simply reflect the onset of significant amounts of magnetite fractionation, which can cause a rapid increase in  $\text{SiO}_2$  content (Garland *et al.*, 1995). Indeed, many of the rhyolites contain magnetite phenocrysts, and diagrams of Nb vs Zr and Y, elements that are incompatible in magnetite, show a nearly continuous trend for the B1 and R1a samples (Fig. 14).

Simple trace-element models provide some useful insights. We were unable to produce model incompatible-element patterns resembling those of the R1 rhyolites by assuming partial melting of solidified B1 basalt with no subsequent fractionation. However, the key features of the Vohitsimbe R1a patterns can be produced at least semi-quantitatively by fractional crystallization of isotopically similar B1 magmas (e.g. Fig. 15a). Partial melting of B1 basalt followed by fractional crystallization of an assemblage of minerals present in these rocks can also yield model patterns with the main features of the Vohitsimbe R1a patterns, but only if the basalt is less evolved than our isotopically appropriate samples (e.g. Fig. 15b). Fits of similar quality are obtained for a range of postulated mineral proportions in the source. No hydrous phases were used in

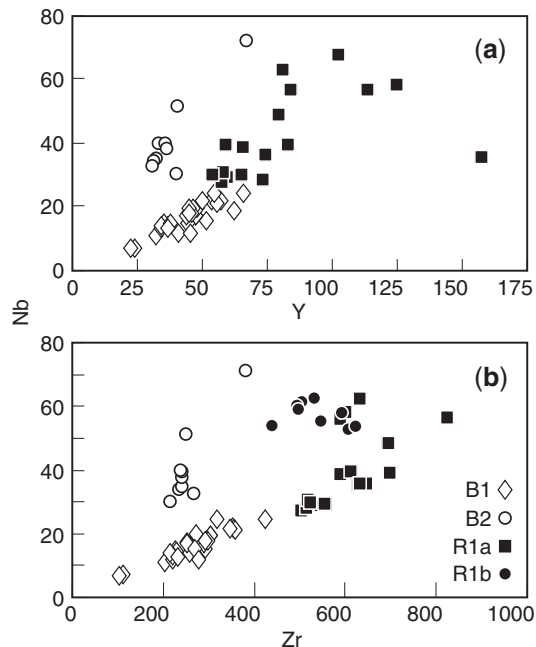
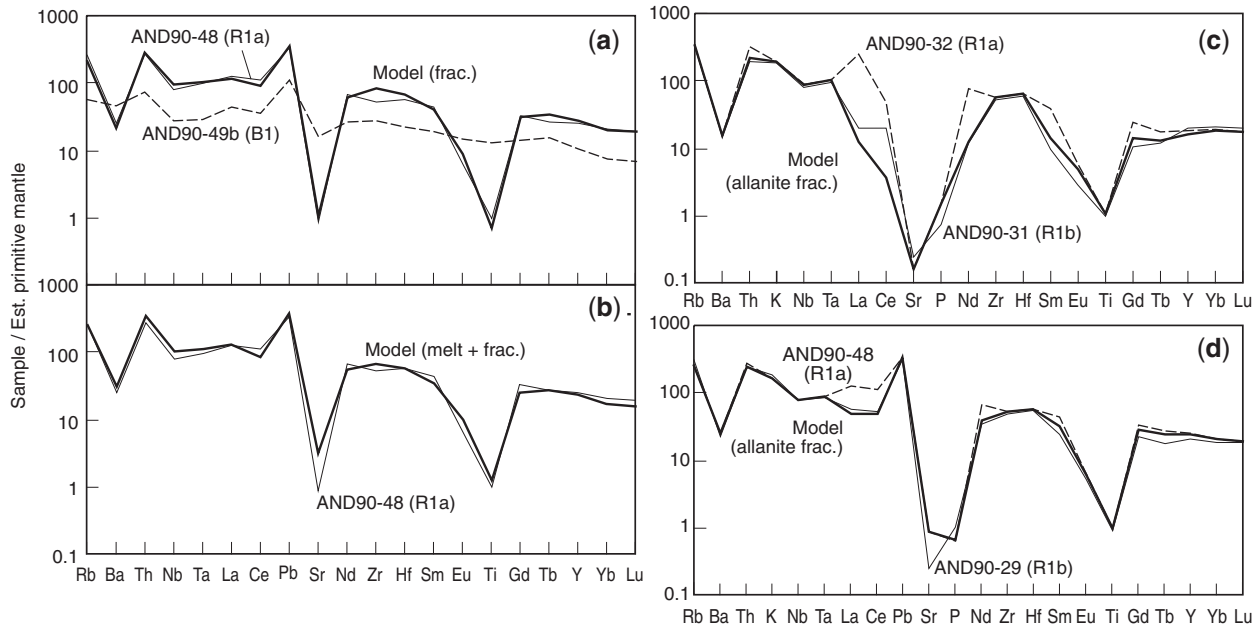


Fig. 14. Nb vs Y (a) and Zr (b) for the B1, B2, R1a and R1b samples.

the modeling, as primary hydrous minerals are lacking in both the R1 rhyolites and basalts; nor were any exotic accessory phases included. The total percentages of fractional crystallization and partial melting are in the ranges estimated in other studies (e.g. Cleverly *et al.*, 1984; Furman *et al.*, 1992; Jónasson *et al.*, 1990; Jónasson, 1994; Cameron *et al.*, 1996; Melluso *et al.*, 2005).

We stress that the examples shown in Fig. 15 should be viewed as illustrative only; they are by no means unique, and such modeling clearly is far too simple to be strictly correct. It assumes a single bulk fractionating assemblage and a single set of constant mineral–melt distribution coefficients, whereas both the fractionating minerals and distribution coefficients change during evolution from basaltic to rhyolitic compositions. Published distribution coefficients for a given rock type vary considerably for some elements (see the Appendix for the values used). Also, even ignoring post-eruptive changes caused by alteration, the basalt samples used in constructing the model patterns are highly unlikely to represent the specific starting compositions from which the actual rhyolites were derived. Errors in any of the above are propagated, and in some cases magnified, through the calculations. Thus, it is difficult to determine whether an origin by fractional crystallization or by partial melting of B1 basalt followed by fractional crystallization is more likely for the Vohitsimbe R1a rhyolites. We note, however, that the amounts of partial melting required in the models are all rather high (25% in the example illustrated in Fig. 15b). The need for a suitable heat source may pose a difficulty in this case, given the >100 km distance of the Androy area from the



**Fig. 15.** (a, b) Key trace-element characteristics of R1a rhyolites with  $\varepsilon_{\text{Nd}}(t) \approx -7$  can be approximated by (a) fractional crystallization of isotopically similar B1 basalt (here, AND90-49b) or (b) partial melting of relatively unevolved, isotopically similar B1 basalt followed by fractional crystallization (here melting of a basalt with incompatible element concentrations 30% lower than those of AND90-49b is assumed). (c, d) Patterns of R1b rhyolites can be approximated by removal of very small amounts of allanite from R1a rhyolites; in (c) 0.13% is removed from AND90-32, and in (d) 0.04% from AND90-48. In (a), the total percentage of fractional crystallization is 75%; the model fractionating assemblage consists of plagioclase, clinopyroxene, magnetite, K-feldspar, and apatite in proportions of 49:31:12:7:1. In (b), 25% of equilibrium melting (Shaw, 1970) of basalt is followed by 45% of fractional crystallization. The model source is 40% plagioclase, 40% clinopyroxene, 10% olivine, and 10% magnetite; melting of these minerals is assumed to occur in proportions of 75:15:5:5, respectively, after Cleverly *et al.* (1984). The subsequent fractionating assemblage is plagioclase, clinopyroxene, magnetite, K-feldspar, and apatite in proportions of 48:5:14:30:3. It should be noted that P and K are not shown in (a) and (b) because these elements are stoichiometric constituents of apatite and K-feldspar, respectively. For simplicity, zircon has not been included in the fractionating assemblages; although evidence for some removal of zircon is present, zircon cannot explain the key incompatible-element differences between the R1a and R1b samples (see text). Distribution coefficients used are given in the Appendix.

zone of major Cretaceous rifting. Indeed, although the analogy with Iceland is imperfect, partial melting of basalt is more important in the formation of Icelandic rhyolites erupted near rift zones, whereas fractional crystallization tends to dominate for rhyolites erupted far from the rift zones (e.g. Selbekk & Trønnes, 2007).

What about the R1b rhyolites? Their incompatible-element patterns are distinctly unlike those of isotopically similar R1a or B1 samples, most notably at Nb–Ta and Zr–Hf, and in the lesser enrichment of the LREE and MREE relative to the HREE (Fig. 8). Their higher average  $\text{SiO}_2$  and the lack of plagioclase phenocrysts in the samples we analyzed by electron microprobe indicate that R1b tends to be more evolved than R1a. Samples AND90-31 and -32 provide an important clue. They were taken from different parts of the same flow, yet AND90-31 has R1b characteristics and AND90-32 is an R1a rhyolite. The differences in the REE suggest control by a REE-rich mineral. Zircon and apatite are two of the more common such phases, and were observed in some of the Androy samples. The large troughs at P in the R1a and R1b (and R2) patterns in Fig. 8 provide strong evidence of apatite control.

Similarly, the nearly constant Zr with increasing  $\text{SiO}_2$  content among the combined R1a and R1b data at  $\text{SiO}_2 > 70$  wt % in Fig. 7g is consistent with at least a minor role for zircon removal in the rhyolite stage of magma genesis; so, too, is the position of several R1b data points to the left of and above the B1–R1a array in Fig. 14b. However, zircon fractionation cannot produce the distinctive humps at Zr–Hf (Fig. 8d) or, because of zircon's greater affinity for HREE vs LREE, the relatively flat slopes of the R1b REE patterns (Fig. 8i). Apatite can produce features qualitatively similar to those observed, but unrealistically large amounts of apatite removal are required; much greater, for example, than permitted by the  $\text{P}_2\text{O}_5$  contents of the Androy samples. However, as illustrated in Fig. 15c, removal from AND90-32 of a tiny amount (0.13%) of allanite, a REE-rich accessory phase common in silicic igneous rocks, produces a pattern very similar to that of AND90-31 (except for Ce, which, as noted above, may have been lowered by alteration in AND90-32). Likewise, Fig. 15d shows that removal of an even smaller amount (0.04%) of allanite from R1a sample AND90-48 produces a pattern closely resembling that of

isotopically similar R1b sample AND90-29. REE concentrations in the rhyolites are in the range estimated for saturation of allanite (Miller & Mittlefehldt, 1983). We did not observe allanite (or monazite or other, more exotic accessory minerals) in thin section, but detection of such phases is difficult because they are never present in more than trace amounts, typically as tiny crystals lining or included in the major phenocrysts (e.g. Miller & Mittlefehldt, 1983; Wolff & Storey, 1984; Michael, 1988). As such, trace minerals such as allanite may largely have been retained along with most of the phenocrysts in the rhyolite magma source.

The R1 samples from stratigraphic levels below the Vohitsimbe section have more negative  $\epsilon_{\text{Nd}}(t)$  ( $-9.4$  to  $-17.3$ ) than measured in the Vohitsimbe R1 rhyolites. Although the actual end-member compositions are unknown, extrapolation of the B2–B1–R1a array in Fig. 12c and the B1–R1 array in Fig. 12d to global average  $(\text{Nb/La})_{\text{pm}}$  and  $(\text{Nb/Pb})_{\text{pm}}$  values of Archean crust suggests a very rough lower limit on  $\epsilon_{\text{Nd}}$  of about  $-25$  for the crustal end-member. However, the offset of the lowest- $\epsilon_{\text{Nd}}(t)$  R1 data to much greater  $(^{87}\text{Sr}/^{86}\text{Sr})_t$  than the lowest- $\epsilon_{\text{Nd}}(t)$  B1 data (Fig. 9a) is accompanied by significantly higher  $(^{208}\text{Pb}/^{204}\text{Pb})_t$ , yet lower  $(^{207}\text{Pb}/^{204}\text{Pb})_t$ , relative to  $(^{206}\text{Pb}/^{204}\text{Pb})_t$  (Fig. 9d and e). These Pb isotope differences indicate that the offset cannot be caused only by differences in coupled fractionation and assimilation during rhyolite vs basalt generation. Rather, these R1 rocks must contain a component of old crust isotopically somewhat different from the low- $\epsilon_{\text{Nd}}$  material affecting the B1 basalts.

Without calling upon any input at all from a basaltic precursor, model fractionated melts of global average Archean intermediate crust yield incompatible-element patterns with characteristics broadly resembling those of the two lowest- $\epsilon_{\text{Nd}}(t)$  rhyolites; that is, those with  $\epsilon_{\text{Nd}}(t)$  of  $-17.0$  and  $-17.3$  (e.g. Fig. 16). The assumptions used in constructing the model pattern in Fig. 16 (40% melting followed by 40% fractional crystallization of plagioclase, clinopyroxene, magnetite, and a small amount of apatite, using the same mineral distribution coefficients as for Fig. 15) are again clearly oversimplifications; also, the specific crustal material involved clearly was not global average Archean crust. Nevertheless, the result suggests that Archean crust may be the overwhelmingly dominant component in the two lowest- $\epsilon_{\text{Nd}}$  rhyolites. Although both orthogneiss and paragneiss are present in the regional basement (Dissanayake & Chandrajith, 1999; Kröner *et al.*, 1999; de Wit *et al.*, 2001), the low  $\text{Al}_2\text{O}_3$  content ( $\approx 11$  wt %) of these rhyolites favors orthogneiss over paragneiss or other aluminous rock of sedimentary origin for this component (e.g. Thy *et al.*, 1990; Beard *et al.*, 1994).

The trachydacites contain less of this crustal component, as indicated by their  $\epsilon_{\text{Nd}}(t)$  values ( $-9.4$  and  $-11.6$ ), but

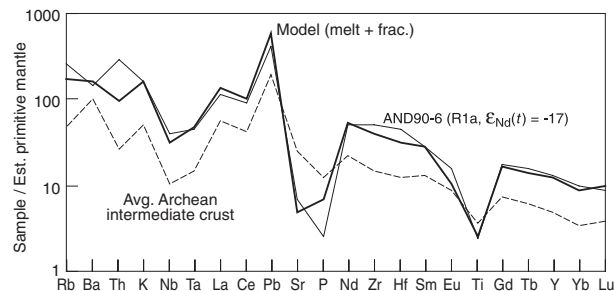


**Fig. 16.** Incompatible-element pattern of low- $\epsilon_{\text{Nd}}(t)$  R1a rhyolite AND90-6 [ $\epsilon_{\text{Nd}}(t) = -17$ ] compared with a model pattern representing 40% of fractional crystallization of a 40% equilibrium melt of global average Archean intermediate crust (Rudnick & Fountain, 1995). The source residue is assumed to consist of 64% plagioclase, 22% clinopyroxene, 13% magnetite, and 1% apatite, after Beard *et al.* (1994). The model fractionating assemblage is plagioclase, clinopyroxene, magnetite, and apatite in proportions of 64:30:5:1, respectively.

more of it than the Vohitsimbe R1 rhyolites. The exact petrogenetic relationship of the trachydacites to the other R1 rocks is unclear, in part because there are so few trachydacites. Data for sample AND90-23 generally lie along or near the ends of trends described by the R1a rhyolites in chemical variation diagrams, broadly consistent with this rock representing a less advanced degree of fractional crystallization in the R1a series. The same appears to be true for the more limited data we have for AND90-22. In contrast, as noted above, AND90-18 is extreme in that it has a deeper Nb–Ta trough, greater  $(\text{La/Yb})_{\text{ch}}$ , and greater concentrations of Zr, Hf, and the MREE and LREE than any of the R1a rhyolites (e.g. Fig. 7g). The high Zr and Hf could indicate a small amount of ‘excess’ zircon in the split of this sample that we used for chemical analysis, but this cannot explain the other features of this unusual sample.

### Group R2

Data for the R2 rhyolites are also offset to higher  $(^{87}\text{Sr}/^{86}\text{Sr})_t$  at similar  $\epsilon_{\text{Nd}}(t)$  relative to the isotopic array defined by the B2 and B1 basalts (Fig. 9a). Unlike the low- $\epsilon_{\text{Nd}}$  R1 samples, however, the R2 data lie consistently between values for the B2 and B1 basalts in Pb–Pb and Nd–Pb isotope space. This feature suggests some sort of petrogenetic relationship to the basalts, and that low- $\epsilon_{\text{Nd}}$  material different from that affecting the basalts is not necessarily required for the R2 rhyolites. That is, their high relative  $(^{87}\text{Sr}/^{86}\text{Sr})_t$  may be a result of coupled assimilation and fractional crystallization in which Sr behaved as a more compatible element than in the basaltic magmas and/or in which the ratio of crystallization rate to assimilation rate was higher. The poorly constrained variables noted in the preceding paragraphs hinder meaningful modeling, but the general effect would be to produce higher  $(^{87}\text{Sr}/^{86}\text{Sr})_t$  for a given  $\epsilon_{\text{Nd}}(t)$  and Pb isotope ratio than in the basalts (James, 1981; DePaolo, 1981). The reason

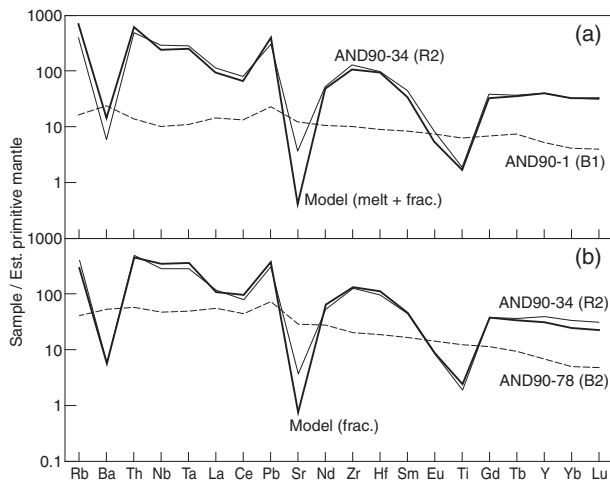


**Fig. 17.** Pattern of R2 rhyolite AND90-34 compared with model patterns for (a) 7% of equilibrium melting of B1 basalt AND90-1 followed by 75% of fractional crystallization, and for (b) 89% of fractional crystallization of B2 basalt AND90-78. The source mineralogy and melting modes in (a) are the same as for Fig. 15b, and the fractionating assemblage is 50% plagioclase, 24% K-feldspar, 17% clinopyroxene, 6% magnetite, 3% apatite, and 0.02% allanite. The assumed fractionating assemblage for (b) is 41% clinopyroxene, 30% plagioclase, 20% K-feldspar, 8% magnetite, 1% apatite, and 0.02% allanite.

is that Sr has a significantly larger bulk distribution coefficient in silicic systems than in basaltic ones, because of the increased importance of feldspar in the fractionating mineral assemblage and because Sr becomes increasingly compatible in feldspar (and several other minerals) as magmatic silica content increases (e.g. Irving, 1978). The deep troughs at Sr in the R2 (and R1) incompatible-element patterns testify that Sr indeed behaved as a rather strongly compatible element during formation of the rhyolites.

The interbedding of R2 and B1 flows at Vohitsimbe (e.g. Fig. 10) suggests the possibility that the R2 rhyolites could be derived from B1 basalt. However,  $\epsilon_{\text{Nd}}(t)$  in the R2 samples is as high as or higher than the highest B1 values; thus, the R2 rhyolites cannot have originated by any combination of assimilation of typical (i.e. low- $\epsilon_{\text{Nd}}$ ) Archean crust and either fractionation or melting of B1 basalt, at least not B1 basalt like any of our samples. If B1-type basalt with higher  $\epsilon_{\text{Nd}}(t)$  was available, could it have been parental to the R2 rhyolites? We were unable to generate R2-like incompatible-element patterns by modeling crystal fractionation of B1 compositions, with or without an added Archean crustal component, principally because concentrations of highly incompatible elements in group B1 are too low relative to those of the less incompatible elements. In contrast, model patterns exhibiting the main features of the R2 patterns can be obtained from fractionated melts of B1 basalt with similar  $\epsilon_{\text{Nd}}(t)$  ( $-3.3$  in AND90-1) to the R2 values ( $-2.0$  to  $-2.6$ ; Fig. 17a). With the distribution coefficients used (Appendix), the chief misfit is at Sr.

As with the R1b rhyolites, the high relative Nb–Ta and Zr–Hf of group R2 can be accounted for by removal of a very small amount of allanite. On this basis, it is possible that the R2 rhyolites were derived from partial melts of high- $\epsilon_{\text{Nd}}$  B1 basalt, coupled with rather extensive fractionation and assimilation of relatively small amounts of ancient crust.

Group B2's higher  $\epsilon_{\text{Nd}}(t)$  values and incompatible-element concentrations, together with its mildly alkalic nature, might seem to make it a better candidate than group B1 for generating the R2 rhyolites. However, combined melting and fractionation models involving <30% partial melting of B2 basalt and assimilation of 0–30% of average Archean mafic, intermediate, or felsic crust did not provide good matches for the R2 incompatible-element patterns. In particular, highly incompatible elements tended to be over-enriched whereas HREE contents were consistently too low. Better fits were achieved by increasing the amount of partial melting to >50%, but melt percentages greater than ~30% are thought to cause disintegration of the basalt protolith, yielding a mafic mush rather than silicic liquid (e.g. Jónasson, 1994). In contrast, advanced crystal fractionation of B2 magma, with or without a small amount of Archean crust, produces a much better fit to the R2 patterns, although HREE concentrations again tend to be rather low (e.g. Fig. 17b).

In short, the trace element evidence appears approximately equally permissive of either a B1-melting (followed by crystal fractionation) origin or a B2-fractionation origin for group R2. A difficulty with deriving the R2 rhyolites via fractionation of B2 basalt, however, is that the B2 flows are confined to the lowermost portion of the volcanic stratigraphy, whereas the R2 rhyolites are in the upper part, within a thick sequence of B1 and R1 flows. Thus, B2-type magma would have had to be present, but unerupted, throughout the Androy episode or else reappear toward the end of volcanism, perhaps in response to decreasing amounts of partial melting in the mantle source. If so, such magmas must not have interacted much with B1 magmas, which were present during eruption of the R2 rhyolites (e.g. Fig. 10).

## CONCLUDING REMARKS

The fact that B1 basalts, R1 rhyolites, and R2 rhyolites are interbedded appears to require the existence of separate, simultaneously active magmatic plumbing systems, at least at the depths where rhyolite generation was occurring. Likewise, at least some interbedding exists between the B2 and R1 flows. We did not find any R2 dikes, but the presence of R1, B1, and B2 dikes indicates that the basalt and R1 rhyolite flows are probably locally derived, which in turn suggests that the different feeder systems were located fairly close to one another. Unfortunately, the mineral assemblages present in the Androy rocks are

not very useful for estimating depths of magma equilibration. The normative compositions of the rhyolites are variable, partly because of alteration, but in the rhyolite tetrahedron (Tuttle & Bowen, 1958) the majority of values for both groups R1 and R2 plot between the 0 and 0.5 GPa cotectics, qualitatively consistent with equilibration at upper-crustal depths. The saucer shape of the Androy structure is consistent with at least one sizeable magma reservoir in the upper crust, whereas the lack of classic caldera-collapse features appears to make a large reservoir at very shallow depths unlikely.

Androy represents the greatest concentration of rhyolite in the Cretaceous system of Madagascar, but far greater volumes of rhyolite were erupted in the Karoo (>35 000 km<sup>3</sup>; Cleverly *et al.*, 1984) and Paraná (>16 000 km<sup>3</sup>; Bellieni *et al.*, 1986; Garland *et al.*, 1995) flood basalt provinces. In both provinces, the rhyolites were formed near the end of volcanism and appear to have erupted largely from zones where crustal extension was greatest. Most of the rhyolite production is attributed to thinning-related decompression and melting of solidified basalt that was underplated earlier to the lower crust. A similar origin may apply for the rhyolites on the central eastern coast of Madagascar, where dikes indicate pre-breakup crustal extension of as much as 20% (M. Storey *et al.*, unpublished data). Like the Karoo and Paraná rhyolites, the Androy rhyolites were formed near the end of the volcanic episode (Storey *et al.*, 1995). However, the Androy massif lies some 100–150 km inland from the rifted margin in a region where extension was limited. Indeed, no major dike swarm transects this area, although the trends of three major swarms converge to the east (Ernst & Buchan, 1997). We infer that extension of basement crust in the Androy area was sufficient to permit repeated intrusion of basaltic magma but limited enough to promote development of relatively stable crustal magma networks and reservoirs where formation of rhyolite could occur through a combination of melting of basalt and magmatic differentiation.

Why some flood basalt provinces produce voluminous rhyolite whereas others (e.g. the Siberian and Deccan Traps) produce only minor rhyolite may ultimately be related to the supply rate of basaltic magma. In many provinces, large-volume flow units of differentiated basalt, commonly in excess of 1000 km<sup>3</sup> (and perhaps as large as 10 000 km<sup>3</sup>; Self *et al.*, 2006), testify to very large, basalt-dominated magma reservoirs. In such systems, formation of rhyolite, by assimilation or fusion of crust or by crystal fractionation, is likely to be swamped by the basaltic component. Only when the input of basaltic magma slows or temporarily stops may more silicic melts begin to dominate a system. However, such melts are likely to be incorporated in the next large batches of mantle-derived melts. Thus, normally we would expect to see eruption of crustally

contaminated basalts, as in the Deccan and Siberian Traps. Until magmatism as a whole begins to die down (for example, when a region moves away from a hotspot), rhyolitic magmas are unlikely to be produced or, if they are, will tend to be incorporated in the more dominant basalt component. The amount of mantle melt that is generated will be a function of lithospheric extension, as well as source temperature and source composition. In south-eastern Madagascar, relatively small amounts of extension were occurring near a probable plume, similar to the situation in the rhyolite-rich Snake River Plain and Yellowstone areas of North America. Fewer rhyolites are found along the rifted eastern margin of Madagascar, where extension was far greater but basalt is abundant. Much of this basalt shows evidence of significant crustal contamination (Storey *et al.*, 1997; J. Mahoney, unpublished data).

Finally, the reason a hotspot-type isotopic signature like that seen in many of the southeastern coastal basalts is lacking at Androy—even though plate reconstructions indicate that the area was near the Marion hotspot at 84 Ma—may also be related to the location of the massif in an area of limited extension. Extension-related thinning and removal of lithospheric mantle was probably less than it was closer to the rifted eastern margin of Madagascar (e.g. see Storey *et al.*, 1997, Fig. 13), leaving more potentially fusible material in the lithospheric mantle beneath Androy and/or permitting greater interaction between lithospheric mantle and magmas ascending from the convecting mantle.

## SUPPLEMENTARY DATA

Supplementary data for this paper are available at *Journal of Petrology* online.

## ACKNOWLEDGEMENTS

We are grateful to A. Razafiniparany for invaluable assistance in arranging permits for the field program, to R. N. Wilson for assistance with the microprobe analysis, and to D. VonderHaar and N. Hulbert for help with other aspects of the work. We thank W. Le Masurier for useful comments, and J. Geldmacher, C. Harris, and L. Melluso for detailed, thoughtful reviews. Funding was provided by the Natural Environment Research Council, UK (GR3/7484) and US National Science Foundation (EAR-9104897).

## REFERENCES

- Annen, C. & Sparks, R. S. J. (2002). Effects of repetitive emplacement of basaltic intrusions on thermal evolution and melt generation in the crust. *Earth and Planetary Science Letters* **203**, 937–955.
- Annen, C., Blundy, & Sparks, R. S. J. (2006). The genesis of intermediate and silicic magmas in deep crustal hot zones. *Journal of Petrology* **47**, 505–539.

- Barker, F. (1981). Introduction to special issue on granites and rhyolites: a commentary for the nonspecialist. *Journal of Geophysical Research* **86**, 10131–10135.
- Battistini, R. (1959). La structure du massif volcanique de l'Androy (Madagascar). *Bulletin de la Société Géologique de France* **7**, 187–191.
- Beane, J. E., Turner, C. A., Hooper, P. R., Subbarao, K. V. & Walsh, J. N. (1986). Stratigraphy, composition and form of the Deccan basalts, Western Ghats, India. *Bulletin of Volcanology* **48**, 61–83.
- Beard, J. S., Lofgren, G. E., Sinha, A. K. & Tollo, R. P. (1994). Partial melting of apatite-bearing charnockite, granulite, and diorite: melt compositions, restite mineralogy, and petrologic implications. *Journal of Geophysical Research* **99**, 21591–21603.
- Belliemi, G., Comin-Chiaromonti, P., Marques, L. S., Melfi, A. J., Nardy, A. J. R., Papatrechas, C., Piccirillo, E. M., Roisenberg, A. & Stolfá, D. (1986). Petrogenetic aspects of acid and basaltic lavas from the Paraná plateau (Brazil): mineralogical and petrochemical aspects. *Journal of Petrology* **27**, 915–944.
- Besairie, H. (1964). *Madagascar, Carte Géologique*. Tananarive: Service Géologique de Madagascar.
- Cameron, K. L., Parker, D. F. & Sampson, D. E. (1996). Testing crustal melting models for the origin of flood rhyolites: a Nd–Pb–Sr isotopic study of the Tertiary Davis Mountains volcanic field, west Texas. *Journal of Geophysical Research* **101**, 20407–20422.
- Cleverly, R. W., Betton, P. J. & Bristow, J. W. (1984). Geochemistry and petrogenesis of the Lebombo rhyolites. In: Erlank, A. J. (ed.) *Petrogenesis of the Volcanic Rocks of the Karoo Province. Geological Society of South Africa Special Publication* **13**, 171–194.
- Cox, K. G. & Hawkesworth, C. J. (1984). Relative contributions of crust and mantle to flood basalt magmatism, Mahabaleshwar area, Deccan Traps. *Philosophical Transactions of the Royal Society of London, Series A* **310**, 627–641.
- DePaolo, D. J. (1981). Trace element and isotopic effects of combined wallrock assimilation and fractional crystallization. *Earth and Planetary Science Letters* **53**, 189–202.
- de Wit, M. J., Bowring, S. A., Ashwal, L. D., Randrianasolo, L. G., Morel, V. P. I. & Rabeloson, R. A. (2001). Age and tectonic evolution of Neoproterozoic ductile shear zones in southwestern Madagascar, with implications for Gondwana studies. *Tectonics* **20**, 1–45.
- Dissanayake, C. B. & Chandrajith, R. (1999). Sri Lanka–Madagascar Gondwana linkage: evidence for a Pan-African mineral belt. *Journal of Geology* **107**, 223–235.
- Doe, B. R., Leeman, W. P., Christiansen, R. L. & Hedge, C. E. (1982). Lead and strontium isotopes and related trace elements as genetic tracers in the upper Cenozoic rhyolite–basalt association of the Yellowstone Plateau volcanic field. *Journal of Geophysical Research* **87**, 4785–4806.
- Dostal, J., Dupuy, C., Nicollet, C. & Cantagrel, J. M. (1992). Geochemistry and petrogenesis of Upper Cretaceous basaltic rocks from southern Malagasy. *Chemical Geology* **97**, 199–218.
- Ernst, R. E. & Buchan, K. L. (1997). Giant radiating dyke swarms: their use in identifying pre-Mesozoic large igneous provinces and mantle plumes. In: Mahoney, J. J. & Coffin, M. F. (eds) *Large Igneous Provinces: Continental, Oceanic, and Planetary Flood Volcanism. American Geophysical Union Monograph* **100**, 297–333.
- Fodor, R. V., Frey, F. A., Bauer, G. R. & Clague, D. A. (1992). Ages, rare-earth element enrichment, and petrogenesis of tholeiitic and alkalic basalts from Kahoolawe Island, Hawaii. *Contributions to Mineralogy and Petrology* **110**, 442–462.
- Furman, T., Frey, F. A. & Meyer, P. S. (1992). Petrogenesis of evolved basalts and rhyolites at Austurhorn, southeastern Iceland: the role of fractional crystallization. *Journal of Petrology* **33**, 1405–1445.
- Garland, F. E., Hawkesworth, C. J. & Mantovani, M. S. M. (1995). Description and petrogenesis of Paraná rhyolites. *Journal of Petrology* **36**, 1193–1227.
- GeoReM (2006). Geological and Environmental Reference Materials Data Base. <http://georem.mpch-mainz.gwdg.de/start.asp>.
- GERM (2006). Geochemical Earth Reference Model. Partition coefficient ( $K_d$ ) database. <http://www.earthref.org>.
- Gunnarsson, B., Marsh, B. D. & Taylor, H. P. (1998). Generation of Icelandic rhyolites: silicic lavas from the Torfajökull central volcano. *Journal of Volcanology and Geothermal Research* **83**, 1–45.
- Haggerty, S. E., Fung, A. T. & Burt, D. M. (1994). Apatite, phosphorus and titanium in eclogitic garnet from the upper mantle. *Geophysical Research Letters* **21**, 1699–1702.
- Harris, C. & Milner, S. (1997). Crustal origin for the Paraná rhyolites: discussion of 'Description and petrogenesis of the Paraná rhyolites, southern Brazil' by Garland *et al.* *Journal of Petrology* **38**, 299–302.
- Harris, C., Whittingham, A. M., Milner, S. C. & Armstrong, R. A. (1990). Oxygen isotope geochemistry of the silicic volcanic rocks of the Etendeka–Paraná province: source constraints. *Geology* **18**, 1119–1121.
- Hart, S. R. (1984). A large-scale isotope anomaly in the Southern Hemisphere mantle. *Nature* **309**, 753–757.
- Hooper, P. R. (1997). The Columbia River flood basalt province: current status. In: Mahoney, J. J. & Coffin, M. F. (eds) *Large Igneous Provinces: Continental, Oceanic, and Planetary Flood Volcanism. American Geophysical Union Monograph* **100**, 1–28.
- Irving, A. J. (1978). A review of experimental studies on crystal–liquid trace element partitioning. *Geochimica et Cosmochimica Acta* **42**, 743–770.
- James, D. (1981). The use of combined oxygen and radiogenic isotopes as indicators of crustal contamination. *Annual Review of Earth and Planetary Sciences* **9**, 311–344.
- Janney, P. E., le Roex, A. P. & Carlson, R. W. (2005). Hafnium isotope and trace element constraints on the nature of mantle heterogeneity beneath the central Southwest Indian Ridge (13°E to 47°E). *Journal of Petrology* **46**, 2427–2464.
- Jónasson, K. (1994). Rhyolite volcanism in the Krafla central volcano, north-east Iceland. *Bulletin of Volcanology* **56**, 516–628.
- Jónasson, K., Holm, P. M. & Pedersen, A. K. (1990). Petrogenesis of silicic rocks from the Króksfjörður central volcano, NW Iceland. *Journal of Petrology* **33**, 1345–1369.
- Kent, R. W., Pringle, M. S., Müller, R. D., Saunders, A. D. & Ghose, N. C. (2002).  $^{40}\text{Ar}/^{39}\text{Ar}$  geochronology of the Rajmahal basalts, India, and their relationship to the Kerguelen Plateau. *Journal of Petrology* **43**, 1141–1153.
- Kirstein, L. A., Peate, D. W., Hawkesworth, C. J., Turner, S. P., Harris, C. & Mantovani, M. S. M. (2000). Early Cretaceous basaltic and rhyolitic magmatism in southern Uruguay associated with the opening of the South Atlantic. *Journal of Petrology* **41**, 1413–1438.
- Kossert, K. (2003). Half-life measurements of  $^{87}\text{Rb}$  by liquid scintillation counting. *Applied Radiation and Isotopes* **59**, 377–382.
- Kröner, A., Windley, B. F., Jaekelt, P., Brewer, T. S. & Razakamanana, T. (1999). New zircon ages and regional significance for the evolution of the Pan-African orogen in Madagascar. *Journal of the Geological Society, London* **156**, 1125–1135.
- Lacroix, A. (1923). *Minéralogie du Madagascar, Volume 3*. Paris: August Challamel.

- Le Bas, M. J., Le Maitre, R. W., Streckeisen, A. & Zanettin, B. (1986). A chemical classification of volcanic rocks based on the total alkali–silica diagram. *Journal of Petrology* **27**, 745–750.
- Leeman, W. P., Oldow, J. S. & Hart, W. K. (1992). Lithosphere-scale thrusting in the western U.S. Cordillera as constrained by Sr and Nd isotopic transition in Neogene volcanic rocks. *Geology* **20**, 63–66.
- Lightfoot, P. C., Hawkesworth, C. J. & Sethna, S. F. (1987). Petrogenesis of rhyolites and trachytes from the Deccan Traps: Sr, Nd and Pb isotope and trace element evidence. *Contributions to Mineralogy and Petrology* **95**, 44–54.
- Lindsley, D. H. & Andersen, D. J. (1983). A two-pyroxene thermometer. *Journal of Geophysical Research* **88**, 887–906.
- Macdonald, G. A. & Katsura, T. (1964). Chemical composition of Hawaiian lavas. *Journal of Petrology* **5**, 2–133.
- Macdougall, J. D. (ed.) (1988). *Continental Flood Basalts*. Dordrecht: Kluwer Academic.
- Mahoney, J. J., Nicollet, C. & Dupuy, C. (1991). Madagascar basalts: tracking oceanic and continental sources. *Earth and Planetary Science Letters* **104**, 350–363.
- Mahoney, J. J., le Roex, A. P., Peng, Z. X., Fisher, R. L. & Natland, J. H. (1992). Southwestern limits of Indian Ocean ridge mantle and the origin of low-<sup>206</sup>Pb/<sup>204</sup>Pb MORB: isotope systematics of the central Southwest Indian Ridge (17°–50°E). *Journal of Geophysical Research* **97**, 19771–19790.
- Mahoney, J. J., White, W. M., Upton, B. G. J., Neal, C. R. & Scrutton, R. A. (1996). Beyond EM-I: lavas from Afanasy–Nikitin Rise and the Crozet Archipelago, Indian Ocean. *Geology* **24**, 615–618.
- Melluso, L., Morra, V., Brotzu, P., Razafiniparany, A., Rattrimo, V. & Razafimahatratra, D. (1997). Geochemistry and Sr-isotopic composition of the Cretaceous flood basalt sequence of northern Madagascar: petrogenetic and geodynamic implications. *Journal of African Earth Sciences* **24**, 371–390.
- Melluso, L., Morra, V., Brotzu, P. & Mahoney, J. J. (2001). The Cretaceous igneous province of central–western Madagascar: evidence for heterogeneous mantle sources, crystal fractionation and crustal contamination. *Journal of Petrology* **42**, 1249–1278.
- Melluso, L., Morra, V., Brotzu, P., D'Antonio, M. & Bennio, L. (2002). Petrogenesis of the Late Cretaceous tholeiitic magmatism in the passive margins of northeastern Madagascar. In: Menzies, M. A., Klemperer, S. L., Ebinger, C. J. & Baker, J. (eds) *Volcanic Rifted Margins*, Geological Society of America, *Special Papers* **362**, 83–98.
- Melluso, L., Morra, V., Brotzu, P., Franciosi, L., Petteruti, Lieberknecht, A. M. & Bennio, L. (2003). Geochemical provinciality in the Cretaceous magmatism of northern Madagascar, and mantle source implications. *Journal of the Geological Society, London* **160**, 477–488.
- Melluso, L., Morra, V., Brotzu, P., Tommasini, S., Renna, M. R., Duncan, R. A., Franciosi, L. & D'Amelio, F. (2005). Geochronology and petrogenesis of the Cretaceous Antampombato–Ambatovy complex and associated dyke swarm. *Journal of Petrology* **46**, 1963–1996.
- Michael, P. J. (1988). Partition coefficients for rare earth elements in mafic minerals of high silica rhyolites: the importance of accessory mineral inclusions. *Geochimica et Cosmochimica Acta* **52**, 275–282.
- Miller, C. F. & Mittlefehldt, D. W. (1983). Depletion of light rare-earth elements in felsic magmas. *Geology* **10**, 129–133.
- Miller, J. A. & Harris, C. (2007). Petrogenesis of the Swaziland and northern Natal rhyolites of the Lebombo rifted volcanic margin, south east Africa. *Journal of Petrology* **48**, 185–218.
- Niu, Y.-L., Waggoner, D. G., Sinton, J. M. & Mahoney, J. J. (1996). Mantle source heterogeneity and melting processes beneath sea-floor spreading centers: East Pacific Rise 18°–19°S. *Journal of Geophysical Research* **101**, 27711–27733.
- O'Hara, M. J. & Mathews, R. E. (1981). Geochemical evolution in an advancing, periodically replenished, periodically tapped, continuously fractionated magma chamber. *Journal of the Geological Society, London* **138**, 237–278.
- Peng, Z. X., Mahoney, J. J., Hooper, P. R., Harris, C. & Beane, J. E. (1994). A role for lower continental crust in flood basalt genesis? Isotopic and incompatible element study of the lower six formations of the western Deccan Traps, India. *Geochimica et Cosmochimica Acta* **58**, 267–288.
- Price, R. C., Gray, C. M., Wilson, R. E., Frey, F. A. & Taylor, S. R. (1991). The effects of weathering on rare earth elements, Y, and Ba in Tertiary basalts from southeastern Australia. *Chemical Geology* **93**, 245–265.
- Riley, T. R., Leat, P. T., Pankhurst, R. J. & Harris, C. (2001). Origins of large volume rhyolitic volcanism in the Antarctic Peninsula and Patagonia by crustal melting. *Journal of Petrology* **42**, 1043–1065.
- Rosholt, J., Prijana, N. & Noble, D. C. (1971). Mobility of uranium and thorium in glassy and crystallized silicic volcanic rocks. *Economic Geology* **66**, 1061–1069.
- Rudnick, R. & Fountain, D. M. (1995). Nature and composition of the continental crust: a lower crustal perspective. *Reviews of Geophysics* **33**, 267–309.
- Salters, V. J. M. & Stracke, A. (2004). Composition of the depleted mantle. *Geochemistry, Geophysics, Geosystems* **5**, Q05004, doi:10.1029/2003GC000597.
- Selbekk, R. S. & Trønnes, R. G. (2007). The 1362 A.D. Öræfajökull eruption, Iceland: petrology and geochemistry of large-volume homogeneous rhyolite. *Journal of Volcanology and Geothermal Research* **160**, 42–58.
- Self, S., Widdowson, M., Thordarson, T. & Jay, A. E. (2006). Volatile fluxes during flood basalt eruptions and potential effects on the global environment: a Deccan perspective. *Earth and Planetary Science Letters* **248**, 517–531.
- Sethna, S. F. & Battiwala, H. K. (1974). Metasomatized basalt xenoliths in the trachyte of Manori–Gorai, Bombay, and their significance. *Geological, Mining and Metallurgical Society of India*, Golden Jubilee Volume 337–346.
- Shaw, D. M. (1970). Trace element fractionation during anatexis. *Geochimica et Cosmochimica Acta* **34**, 237–243.
- Sigmarsson, O., Hémond, C., Condomines, M., Fourcade, S. & Oskarsson, N. (1991). Origin of silicic magma in Iceland revealed by Th isotopes. *Geology* **19**, 621–624.
- Snyder, D. (2000). Thermal effects of the intrusion of basaltic magma into a more silicic magma chamber and implications for eruption triggering. *Earth and Planetary Science Letters* **175**, 257–273.
- Sobolev, A. V., Hofmann, A. W., Sobolev, S. V. & Níkogosian, I. K. (2005). An olivine-free mantle source of Hawaiian shield basalts. *Nature* **434**, 590–597.
- Storey, M., Mahoney, J. J., Saunders, A. D., Duncan, R. A., Kelley, S. P. & Coffin, M. F. (1995). Timing of hotspot-related volcanism and the breakup of Madagascar and India. *Science* **267**, 852–855.
- Storey, M., Mahoney, J. J. & Saunders, A. D. (1997). Cretaceous basalts in Madagascar and the transition between plume and

- continental lithosphere mantle sources. In: Mahoney, J. J. & Coffin, M. F. (eds). *Large Igneous Provinces: Continental, Oceanic, and Planetary Flood Volcanism. American Geophysical Union Monograph* **100**, 95–122.
- Stormer, J. C. & Nicholls, J. (1978). XLFAC: a program for the interactive testing of magmatic differentiation models. *Computers and Geosciences* **4**, 143–159.
- Sun, S.-S. & McDonough, W. F. (1989) Chemical and isotopic systematics of oceanic basalts: implications for mantle composition and processes. In: Saunders, A. D. & Norry, M. J. (eds) *Magmatism in the Ocean Basins. Geological Society, London, Special Publications* **42**, 313–345.
- Thy, P., Beard, J. S. & Lofgren, G. E. (1990). Experimental constraints on the origin of Icelandic rhyolites. *Journal of Geology* **98**, 417–421.
- Todt, W., Cliff, R. A., Hanser, A. & Hofmann, A. W. (1996). Evaluation of a  $^{202}\text{Pb}$ – $^{205}\text{Pb}$  double spike for high-precision lead isotopic analyses. In: Basu, A. & Hart, S. (eds) *Earth Processes: Reading the Isotopic Code. American Geophysical Union Monograph* **95**, 429–437.
- Torsvik, T. H., Tucker, R. D., Ashwal, L. D., Eide, E. A., Rakotosolofo, N. A. & de Wit, M. J. (1998). Late Cretaceous magmatism in Madagascar: palaeomagnetic evidence for a stationary Marion hotspot. *Earth and Planetary Science Letters* **164**, 221–232.
- Tuttle, O. F. & Bowen, N. L. (1958). Origin of granite in the light of experimental studies in the system  $\text{NaAlSi}_3\text{O}_8$ – $\text{KAlSi}_3\text{O}_8$ – $\text{SiO}_2$ – $\text{H}_2\text{O}$ . *Geological Society of America, Memoirs* **74**.
- Wolff, J. A. & Storey, M. (1984). Zoning in highly alkaline magma bodies. *Geological Magazine* **21**, 563–575.
- Wooden, J. L., Czamanske, G. K., Fedorenko, V. A., Arndt, N. T., Chauvel, C., Bouse, R. M., King, B. S. W., Knight, R. J. & Siems, D. F. (1993). Isotopic and trace-element constraints on mantle and crustal contributions to Siberian continental flood basalts. Noril'sk area, Siberia. *Geochimica et Cosmochimica Acta* **57**, 3766–3704.
- Yoder, H. S., Jr (1973). Contemporaneous basaltic and rhyolitic magmas. *American Mineralogist* **58**, 153–171.
- York, D. (1969). Least-squares fitting of a straight line with correlated errors. *Earth and Planetary Science Letters* **5**, 320–324.

## APPENDIX: MINERAL–LIQUID DISTRIBUTION COEFFICIENTS USED FOR RHYOLITE MODELING

Element	Plagio-clase	Clino-pyroxene	Olivine	Magnetite	K-feldspar	Apatite	Allanite
Rb	0.01	0.0005	0	0.01	0.5	0.4	0.19
Ba	0.23	0.0005	0	0.08	7	0.4	5
Th	0	0.0003	0.0001	0.1	0.01	1	283
U	0	0.0004	0.0001	0.1	0.01	1	14
K	0.17	0.005	0.001	0.01	SC	0.4	0.2
Nb	0.1	0.01	0	0.4	0.15	0.1	1.7
Ta	0.1	0.01	0	0.4	0.15	0.1	1.7
La	0.17	0.01	0.0001	0.46	0.07	8	2360
Ce	0.12	0.163	0.0001	0.7	0.04	10	2060
Pb	0.2	0.01	0.0001	0	1	0.03	0.7
Sr	1 (5)	0.26	0.016	0.05	5	5	1.8
P	0.05	0.256	0.0002	0.1	0	SC	0.2
Nd	0.081	0.288	0.0003	0.75	0.02	13	1400
Zr	0.08	0.3	0.01	0.8	0	2	0.29
Hf	0.08	0.3	0.005	0.8	0	2	9.8
Sm	0.067	0.35	0.0006	0.71	0.01	19	756
Eu	0.8 (1.5)	0.38	0.005	0.45	2	18	100
Ti	0.01	0.3	0.016	20	0	0.1	0.1
Gd	0.063	0.41	0.009	0.75	0.02	15	400
Tb	0.059	0.44	0.013	0.75	0.03	15	235
Y	0.03	0.485	0.01	0.2	0	10	95.5
Yb	0.067	0.467	0.03	0.3	0.01	9	24.5
Lu	0.067	0.45	0.034	0.3	0.01	8	22

For plagioclase, the coefficients for Sr and Eu shown in parentheses were used for modeling fractional crystallization to rhyolite compositions; coefficients not in parentheses were used for modeling partial melting of mafic or intermediate crust. SC, stoichiometric constituent. Distribution coefficients are from the GERM website (GERM, 2006; <http://www.earthref.org>).